FLOW DYNAMICS OF COMPLEX FLUIDS USING NUMERICAL MODELS

BY

Amir Shakib-Manesh

Academic Dissertation

for the Degree of

Doctor of Philosophy

To be presented, by permission of the
Faculty of Mathematics and Natural Sciences
of the University of Jyväskylä,
for public Examination in Auditorium FYS-1 of the
University of Jyväskylä on December 2, 2003
at 12 o'clock noon

Jyväskylä, Finland
November, 2003

PREFACE

This work has been carried out during the years 1998-2002 mainly in the Department of Physics, University of Jyväskylä. I wish to thank my supervisors Prof. Jussi Timonen and Prof. Markku Kataja for guidance and support. Special thanks are due to Dr Jan Åström, Dr Antti Koponen, Dr Juha Merikoski, Dr. Jussi Maunuksela, Mr. Pasi Raiskinmäki and Mr. Ari Jäsberg for their valuable collaboration and advice. I would also like to thank Prof. Piroz Zamankhan who invited me to Finland, was my supervisor in the first publication of this Thesis, and thereby introduced me to the world of physics.

I would like to thank my parents to whose support I owe my successes, the people of the Department of Physics, and all my near friends.

Jyväskylä, November 2003

Amir Shakib-Manesh

ABSTRACT

In this thesis several multiphase flow problems with complex boundaries have been analyzed numerically: granular flows, capillary rise and rheological properties of particulate suspensions.

We analyze the long-time diffusion coefficient in the shear flow of inelastic, rough, hard granular spheres by molecular dynamics simulations, and observe a transition from a disordered to a layered state at solid volume fraction $\phi_s = 0.565$. This transition causes a sharp drop in the long-time transverse self-diffusion coefficient of particles.

We verify that the two-phase lattice-Boltzmann method applied here is capable of modelling the capillary rise phenomenon. We also demonstrate the dependence of the dynamic contact angle on the capillary number, and the applicability of the Washburn equation when changing contact angle is properly included.

Several benchmark studies are carried out to validate the lattice-Boltzmann code developed for liquid-particle suspensions in the non-Brownian regime. The main emphasis in this comparison is on the dependence of the viscosity of the suspension on the concentration of particles. We then analyze in more detail the dependence of viscosity on shear rate in a Couette flow geometry. The onset of shear thickening is found to be related to a maximum in the layering of particles near the channel walls. A comprehensive study of the various momentum transfer mechanisms that contribute to the total shear stress indicates that both these phenomena are related to enhanced relative solid-phase stress. The apparent viscosity of the suspension is found to be completely given by the ratio of the solid-phase stress to the total stress, and this dependence takes the form of a simple rational function.

We finally analyze the low Reynolds number flow of 2D liquid-particle suspensions, in which suspended particles may attach on channel walls, and deposited particles are detached if the hydrodynamic force on them exceeds a given threshold. The behaviour of this system is controlled by concentration of particles and detachment threshold. At low values of these parameters there is no deposition on the walls, followed by a first-order like transition to a phase in which deposition layers exist in the stationary state. Close to the transition, these layers display a meandering pattern whose wavelength is directly proportional to suspension velocity. The meandering phase is followed by a necking phase in which deposition layers still do not block the flow channel. Finally a transition to a fully blocked flow channel takes place. This last transition is driven by equilibrium fluctuations in the deposition layers.

Keywords: Multiphase flows, lattice Boltzmann, suspension, rheology, pipe clogging.

LIST OF PUBLICATIONS

I. P. Zamankhan, W. Polashenski Jr., H. Vahedi Tafreshi, A. Shakib-Manesh, P. J. Sarkomaa, Shear-Induced particle diffusion in inelastic hard sphere fluids, Phys. Rev. E **58**, R5237 (1998).

II. P. Raiskinmäki, A. Shakib-Manesh, A. Koponen, A. Jäsberg, J. Merikoski and J. Timonen, Lattice-Boltzmann simulation of capillary rise dynamics, J. Stat. Phys. **107**, 147 (2002).

III. P. Raiskinmäki, A. Shakib-Manesh, A. Koponen, A. Jäsberg, M. Kataja and J. Timonen, Simulation of non-spherical particles suspended in a shear flow, Comp. Phys. Comm. **129**, 185 (2000).

IV. A. Shakib-Manesh, P. Raiskinmäki, A. Koponen, M. Kataja and J. Timonen, Shear stress in a Couette flow of liquid-particle suspensions, J. Stat. Phys. **107**, 67 (2002).

V. A. Shakib-Manesh, J.A. Åström, A. Koponen, P. Raiskinmäki and J. Timonen, Fouling dynamics in suspension flows, Eur. Phys. J. E **9**, 97 (2002).

The author of the thesis has participated in the formulation of the problem, numerical analysis of the results and preparation of the article [I]. The author has written the first draft of the articles IV,V, and also written selected parts of the articles II,III. The author has performed almost all of the numerical computations needed, and participated in the formulation of the problems, and the development of the analytial models.

CONTENTS

1 INTRODUCTION

Multiphase fluids or so-called 'complex fluids' are common in daily life. The term 'multiphase fluids', which has been used for less than half a century [1], stands for systems with different substances or different phases of matter (solid, liquid or gas) in coexistence. Multiphase flow regimes can appear as dispersed regimes (*i.e.* not materially connected) such as particle, droplet or bubbly flows. Other forms of dispersed multiphase flow regimes are slug flow (large bubbles in a continuous fluid), annular flow (continuous fluid along walls, gas in the center), and stratified flow (immiscible fluids separated by identifiable interfaces) [2]. There are also non-dispersed multiphase flows such as fluid flow through a porous material. Multiphase fluids have more complicated microstructure than single fluids and their flow dynamics depend on many physical parameters.

Study of complex fluids is important for several reasons. Flow processes of complex fluids are encountered in numerous applications in many industries and in nature. Design and operation of multiphase processes call for understanding the basic mechanisms involved. This understanding is seldom available simply because of the complicated behaviour of multiphase materials. Therefore, studies of simple multiphase processes are needed as first steps towards handling of realistic problems.

So far, perhaps apart from turbulence, the dynamics of single-phase fluids is fairly well understood. However, there is a large number of unsolved fundamental problems related to the macroscopic properties of multiphase materials. A primary difficulty in many multiphase flow problems involves the prediction of the shape and position of the interface between different phases. Experimental techniques are often not designed for multiphase systems and have difficulties to accurately probe the flow properties.

In practice, the underlying multiphase character is often neglected, and the system is treated formally as a single-phase 'rheological' or 'non-Newtonian' fluid. In many applications with low volume fraction of particles, droplets, or bubbles, the system may indeed behave like a single-phase fluid. However, if concentration of the dispersed phase increases, significant changes may appear in the physical behaviour. For example, in a single-phase fluid the transfer of momentum simply results from internal motion or interaction of fluid particles, while in multiphase

fluids such as suspensions, viscosity, the resistance of the fluid to flow, arises from many mechanisms that involve interactions between the different phases.

This thesis addresses several mesoscopic multiphase problems and is based on molecular and mesoscopic fluid dynamics simulations. Two major problems are discussed.

On the one hand, the effect of shear on the dynamical and equilibrium properties, the microstructure and the rheological behaviour of monodisperse granular media and liquid-particle suspensions are discussed.

First we investigate in detail the three-dimensional bounded and sheared granular flow by using direct numerical simulations. The main emphasis of this study is on the diffusion and microstructural behaviour of such materials under shear deformation. Concentrated suspensions behave similarly to these dense granular media, but with more complex microstructure and dynamics, due to the existence of fluid between the suspended particles.

One of the major questions in the rheological behaviour of sheared particulate suspensions is whether they display a dilatant rheological behaviour. Industrial applications that involve this problem include mixer blade damage or bowing of roller in milling operations, slurry fractures, and rupture of coating material in paper industry. It would also be important to better understand the operation of common viscometers. We have thus studied the rheological behaviour of sheared two- or three-dimensional non-Brownian liquid-particle suspensions using numerical techniques. This study includes the effect of shear deformation on the microstructure of the suspension and on the transport coefficients such as viscosity. We also analyze various momentum transfer mechanisms, and their contribution in the formation of viscosity.

On the other hand, Poiseuille flow of fluids is examined without and with suspended colloidal particles. The former case, the pipe flow of a fluid, is related *e.g.* to flow in porous materials, as narrow pores behave like capillary pipes. In a capillary pipe containing two immiscible fluids, pressure difference across the interface between these fluids (capillary pressure) makes the denser fluid rise inside the capillary even if there is an opposing external force such as gravity. Using numerical simulations of a two-phase fluid, we study this capillary phenomenon, *e.g.* the dynamics of the fluid-solid contact angle. By studying the capillary rise, we can also benchmark our numerical techniques for modelling imbibition of fluid in a gas-filled porous medium.

We also study small-Reynolds-number pipe flow of a particle suspension, where the particles can deposit on channel walls, and deposited particles are detached if the hydrodynamic force on them is above a threshold value. The behaviour of this system is determined by two parameters: the concentration of the suspension and the detachment threshold, and it has a rich phase diagram. Possible applications of the problem extend from clogging of tiny blood veins in the human body, and

blockage of narrow capillaries in coating colour slurries, to fouling of pipes in petroleum industry.

In the analysis of the problems described above, two numerical methods were used. The molecular dynamics method was first used to simulate the dynamics of hard spheres [3], but since then it has been extended to many other more complicated systems [4,5,6]. This method is a powerful tool in many physical problems, and it has been used to analyze *e.g.* rapid flows in a high Reynolds number regime of granular media [7], dilatancy phenomena [8] and fluidization of grains [9]. We use this method to analyze sheared granular flow.

For modelling complex fluids with moving internal boundaries, mesoscale methods like coarse-grained particle-based schemes (such as DPD) [10] or lattice-based methods (such as the lattice-Boltzmann method [11,12,13,14] (LBM) and lattice-gas cellular automata [15,16,17,18]), are usually better than the conventional CFD methods [19]. LBM can also be seen as a special finite-difference scheme for the kinetic equation of a discrete velocity distribution function. It has evolved in recent years into an alternative and promising scheme for simulating various fluid flows [13, 19 ,20,21], and we use this method extensively in this thesis.

2 NUMERICAL METHODS

2.1 WHY COMPUTER SIMULATIONS?

Modelling can be done by means of theory, laboratory prototypes, or numerical techniques. The theoretical models often use, especially in complicated many-body problems, macroscopic equations to describe the physical phenomenon at hand, thereby neglecting many microscopic details of the system. Numerical methods usually lack this problem, and they are normally inexpensive in comparison with laboratory experiments. Numerical methods also provide efficient benchmarks for theoretical models. They can address details of complex phenomena that can be difficult for theory as well as for experiments.

Experimental difficulties may arise from complexity, expenses, danger or hazardous condition of the phenomenon. For example, in a dense suspension flow, measuring of the local instantaneous flow quantities such as velocities and stresses, separately for both phases, is not feasible. Such information can however be attained from numerical simulations of the suspension flow. Also, numerical techniques are versatile enough to combine or distinguish different physical phenomena, which have made them popular tools of analysis.

The results of numerical techniques are however subject to uncertainties that arise from *e.g.* the flow model and the numerical techniques used. Care must therefore be taken when expressing the results of numerical simulations, and they should be supported by theoretical and/or experimental benchmarks.

In this thesis mainly two numerical techniques have been used for simulation of flow problems, especially multiphase phenomena, starting from microscale molecular dynamics of spherical particles up to mesoscale simulations of capillary rise phenomena, shear or Poiseuille flow of suspension, and clogging of suspension flow in channels. In each case, experimental or theoretical evidence have been used for benchmarking the method.

2.2 NUMERICAL SIMULATIONS AT DIFFERENT RELEVANT LENGTH SCALES

In colloidal suspensions, for example, there are three important length scales, the microscopic size of the relevant molecules, the mesoscopic scale related to the size of colloidal particles, and the macroscopic scale which is that of the effective fluid motion. In particulate suspensions the size of the suspended particles can be in the macroscopic scale.

As the relevant length scales in suspensions differ by several orders of magnitude, it is not possible to simulate them by including details at all these length scales. All numerical methods are based on one basic length scale. For macroscopic modelling the suspension must be regarded as a continuum medium, and the description is in terms of the variations of the macroscopic velocity, density and pressure (and temperature) with space and time.

The macroscopic scale simulations, which usually go under the general name of computational fluid dynamics [22,23] (CFD), use macroscopic continuum equations like the Navier-Stokes equation, whose solutions are very sensitive to the boundary conditions. Various CFD methods offer successful simulation tools for different single-phase fluid dynamics problems within many branches of science and engineering [24]. For suspensions however, these methods are difficult to apply due to the moving boundaries of the suspended particles. In recent finite-element simulations it has been possible to analyse only cases with small numbers of particles [25,26], or simulations were limited to simple and regular particle geometries [27,28].

An attempt to circumvent the problems with moving or otherwise complex boundaries is provided by lattice-based methods which are based on a mesoscopic basic unit of the system, typically of the order of a micrometer, but depending of course on the details of the system. There are a few popular methods, which use this approach, and they include the lattice-gas automata (LGA), its alteration the lattice-Boltzmann method (LBM) and the method of dissipative particle dynamics (DPD). Each of these methods has its advantages and limitations. Use of mesoscale simulation techniques can allow the exact treatment of small-scale macroscopic systems, and can be used to effectively study *e.g.* the rheology of colloidal suspensions and the dynamics of interfaces. Simulations at the microscopic level have also been attempted in order to understand the truly microscopic behaviour of liquids.

As Monte Carlo simulations are not suitable to describe the dynamic properties [29], the prevalent microscopic simulation method is that of molecular dynamics (MD) [3]. MD methods that apply different numerical techniques have thus been developed to study the dynamical behaviour of a large number of applications, see *e.g.* [29,30,31,32,33]. MD simulations are computationally very demanding, and obtaining bulk properties of, for example, suspensions, would mean using billions of particles [34].

We review below in more detail the MD method and the LB method used in this work.

2.3   THE MOLECULAR DYNAMICS METHOD

Molecular dynamics (MD) provides a reasonable physical description of granular materials including their macroscopic averaged properties, hydrodynamics, and all fluctuations, using only linear dynamics.

A (granular) system of spheres is initialised by first randomly placing the spheres in a box. Then overlapping spheres are randomly moved until no overlaps remain. Thereafter the system evolves in time according to Newton's equations of motion under chosen initial and boundary conditions, and applied forces and fields.

Four major steps are needed to enrol a hard-sphere molecular dynamics simulation: motion control, determination of collision times, collision dynamics, and calculation of the particle properties.

2.3.1   Motion control

The motion of a rigid body of mass m and acceleration $\mathbf{a} = \mathbf{F}/m$, due to an external force $\mathbf{F}$, follows Newton's Second Law. The total kinetic energy and momentum of the system must be conserved, as well as its total angular momentum

$$\mathbf{J} = \sum_i m\mathbf{r}_i \times \mathbf{v}_i + \sum_i I\boldsymbol{\omega}_i, \tag{2.1}$$

where $\mathbf{r}_i$ is the position, $\mathbf{v}_i$ the velocity and $\boldsymbol{\omega}_i$ the angular velocity of particle i. I is the moment of inertia of the particles, which is $2mR^2/5$ for a sphere and $mR^2/2$ for a disk, with R the respective radius of the particle.

Verlet algorithm

For the positions $\mathbf{r}$ the most popular time integration algorithm is the so-called Verlet algorithm. Forward and backward Taylor expansions of the position as a function of time can be written in the forms

$$\mathbf{r}(t+\delta t) = \mathbf{r}(t) + \delta t \mathbf{v}(t) + (1/2)\delta t^2 \mathbf{a}(t) + O(\delta t^3),$$
$$\mathbf{r}(t-\delta t) = \mathbf{r}(t) - \delta t \mathbf{v}(t) + (1/2)\delta t^2 \mathbf{a}(t) + O(\delta t^3). \tag{2.2}$$

Adding the above two expressions gives the new position after time δt,

$$\mathbf{r}(t+\delta t) = 2\mathbf{r}(t) - \mathbf{r}(t-\delta t) + \delta t^2 \mathbf{a}(t) + O(\delta t^3). \tag{2.3}$$

There are several methods to make Eq. (2.3) explicit, the most common of these being the so-called half-step 'leap-frog' scheme [31],

$$\mathbf{r}(t+\delta t) = \mathbf{r}(t) + \delta t \mathbf{v}(t+\delta t/2). \tag{2.4}$$

So the velocity of the mid-step may be written as

$$\mathbf{v}(t+\delta t/2) = \mathbf{v}(t-\delta t/2) + \frac{\mathbf{F}(t)}{m}\delta t. \tag{2.5}$$

Similarly for the angle (orientation) of a particle (in the case of non-spherical particles)

$$\boldsymbol{\theta}(t+\delta t)=\boldsymbol{\theta}(t)+\delta t\boldsymbol{\omega}(t+\delta t/2), \tag{2.6}$$

and for its angular velocity

$$\boldsymbol{\omega}(t+\delta t/2)=\boldsymbol{\omega}(t-\delta t/2)+\frac{\mathbf{T}(t)}{I}\delta t. \tag{2.7}$$

Later during the step, the current velocities are determined from

$$\mathbf{v}(t)=\frac{1}{2}\big(\mathbf{v}(t+\delta t/2)+\mathbf{v}(t-\delta t/2)\big), \tag{2.8}$$

and similarly for the angular velocities.

2.3.2 Collision procedures

Collision time

Consider two smooth hard spheres with relative locations $\mathbf{r}_{ij}=\mathbf{r}_i-\mathbf{r}_j$ and velocities $\mathbf{v}_{ij}=\mathbf{v}_i-\mathbf{v}_j$ (see Figure 2.1).
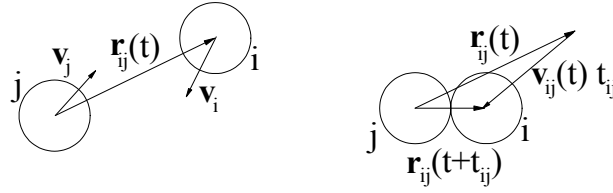

Figure 2.1 Smooth hard-sphere collision: situation before and at the collision moment.

At the collision moment, the particle-particle distance should be equivalent to the particle diameter [29],

$$\left|\mathbf{r}_{ij}\left(t+t_{ij}\right)\right|=\left|\mathbf{r}_{ij}\left(t\right)+\mathbf{v}_{ij}\left(t\right)t_{ij}\right|=2R. \tag{2.9}$$

Rearranging this expression gives a quadratic equation for the time to collision,

$$t_{ij}^2+\frac{2b_{ij}}{v_{ij}^2}t_{ij}+\frac{r_{ij}^2-\left(2R\right)^2}{v_{ij}^2}=0 \tag{2.10}$$

with $b_{ij}\equiv\mathbf{r}_{ij}\cdot\mathbf{v}_{ij}$. One can see that Eq. (2.10) is very important in collision detection:

$$\begin{cases} b_{ij}>0 \;;\; no\;\;collision\;\;takes\;\;place, \\ b_{ij}<0\;\;and\;\;\sqrt{\left(b_{ij}^2-v_{ij}^2\left(r_{ij}^2-4R^2\right)\right)}<0;\;no\;\;collision\;\;takes\;\;place, \\ b_{ij}<0\;\;and\;\;\sqrt{\left(b_{ij}^2-v_{ij}^2\left(r_{ij}^2-4R^2\right)\right)}\geq0;\;collision\;\;takes\;\;place. \end{cases} \tag{2.11}$$

The solution of Eq. (2.10) gives the minimum collision time [29],

$$t_{ij}=\frac{-b_{ij}\pm\sqrt{b_{ij}^2-v_{ij}^2\left(r_{ij}^2-4R^2\right)}}{v_{ij}^2}. \tag{2.12}$$

Of the two roots of solution (2.12), the smaller one obviously gives the minimum time to collision between the two particles.

Collision dynamics

At the moment of collision, the total momentum should conserve, *i.e.*,

$$\mathbf{v}'_i = \mathbf{v}_i - \delta\mathbf{P}^n_{ij}/m,$$
$$\mathbf{v}'_j = \mathbf{v}_j + \delta\mathbf{P}^n_{ij}/m. \tag{2.13}$$

Here for smooth particles, $\delta\mathbf{P}^n_{ij}$ is the projection of relative momentum $m\mathbf{v}_{ij}$ along the vector $\mathbf{r}_{ij}$, *i.e.*,

$$\delta\mathbf{P}^n_{ij}/m = \left(\frac{\mathbf{r}_{ij}\cdot\mathbf{v}_{ij}}{4R^2}\right)\mathbf{r}_{ij}. \tag{2.14}$$

For smooth particles (with frictionless surface) the post-collision components of velocities perpendicular to the vector $\mathbf{r}_{ij}$ remain unchanged as well as their angular velocities. However, for rough particles (see definition below Eq. (2.17)) one can derive [29]

$$\delta\mathbf{P}_{ij}/m = \frac{1}{2}\left[\left(2\mathbf{v}_{ij}\right)_n + \frac{I}{mR^2+I}\left(2\mathbf{v}_{ij}\right)_t\right]. \tag{2.15}$$

In the case of rough particles, the particles have a no-slip contact [35] and therefore the post-collisional velocities in the normal and tangential directions are

$$\mathbf{v}'_n = -e\,\mathbf{v}_n,$$
$$\mathbf{v}'_t = -\beta\,\mathbf{v}_t. \tag{2.16}$$

where e and β are the normal and tangential coefficients of restitution. β can be expressed in terms of e and the friction coefficient μ such that

$$\beta = -1 + \mu(1+e)\left(1+mR^2/I\right)v_n/v_t. \tag{2.17}$$

The post-collision velocities and angular velocities can now be derived in a similar way to Eq. (2.13). While e varies between 0 and 1, corresponding to change from inelastic to fully elastic material, β varies between –1 to +1 corresponding to change from a perfectly smooth to a perfectly rough particle. For more details concerning the collision event, geometry of the system and simulation algorithm, see [29,36].
The angular velocities for rough particles are determined from

$$\boldsymbol{\omega}'_i = \boldsymbol{\omega}_i + \mathbf{r}_{ij}\times\delta\mathbf{P}_{ij}/2I,$$
$$\boldsymbol{\omega}'_j = \boldsymbol{\omega}_j + \mathbf{r}_{ij}\times\delta\mathbf{P}_{ij}/2I. \tag{2.18}$$

Note that in the case the particles are not spherical, the vector $\mathbf{r}_{ij}$ is normal to the tangential plane at the contact point between the two colliding particles.

2.3.3   Structural information

When analysing systems of particles that undergo Newtonian dynamics, it is important to infer also structural features of the system. This is important in particular when systems with high solid volume fraction are considered, as in these

systems phase transition to ordered states may appear. We therefore explain briefly the main tools for the analysis of structural order.

Radial distribution function

The radial distribution function (pair correlation function) measures correlation in the density of particles. It can be defined as the probability of finding another particle at distant r from a particle [37], and can be expressed in the form

$$g(r) = \frac{V}{4\pi r^2 N^2} \left\langle \sum_i^N \sum_{i \neq j}^N \delta\left(\mathbf{r}(t) - \mathbf{r}_{ij}(t)\right) \right\rangle, \tag{2.19}$$

where V is the volume of the system, δ the Dirac delta function and the angular brackets denote configurational average.

Translational order

Translational order appears as periodicity in the particle density, and can thus be described by Fourier components $\rho_\mathbf{k}(t)$ of the mass density [38],

$$\rho_\mathbf{k}(t) = \frac{1}{N} \sum_{i=1}^N \rho_\mathbf{r}(t) \cos(\mathbf{k} \cdot \mathbf{r}_i), \tag{2.20}$$

Here wave vector $\mathbf{k}$ is such that $k \leq 2\pi/V^{1/3}$, which becomes a reciprocal lattice vector for a regular lattice $\{\mathbf{r}\}$.

Bond orientational order

Orientational order can best be parameterized with spherical harmonics, and we thus consider the quantity $Q_{lm}(\mathbf{r}) \equiv Y_{lm}(\theta(\mathbf{r}), \phi(\mathbf{r}))$ [39], where $Y_{lm}(\theta(\mathbf{r}), \phi(\mathbf{r}))$ is a spherical harmonics with $\theta(\mathbf{r})$ and $\phi(\mathbf{r})$ the polar and azimuthal angle, respectively, and $\{\mathbf{r}\}$ is the set of midpoints of bonds between all nearest-neighbour (nn) particles. An order parameter which measures orientational order, can thus be defined as

$$Q_l = \left(\frac{4\pi}{2l+1} \sum_{m=-l}^l \left| \overline{Q}_{lm} \right|^2 \right)^{1/2}, \tag{2.21}$$

where $\overline{Q}_{lm} \equiv \frac{1}{N_{bond}} \sum_{\alpha=1}^{N_{bond}} Q_{lm}(\mathbf{r}_\alpha)$, and the average is taken over all nn bonds of the sample.

l	2	4	6	8	10
SC (7-atom)	0	0.75	0.40	0.75	0.40
BCC (15-atom)	0	0.05	0.55	0.50	0.20
FCC (13-atom)	0	0.20	0.60	0.40	0.05
HCP (13-atom)	0	0.15	0.55	0.40	0.05
ICOS (13-atom)	0	0	0.60	0	0.40

Table 2.1 Approximate values for Q_l [39].

Bond-angle correlation functions

Bond-angle correlation functions $G_l(\mathbf{r})$ measure the flexibility with which a bond can have local orientations in a given state. It can be defined as

$$G_l(\mathbf{r}) = \frac{4\pi}{2l+1} \sum_{m=-l}^{l} \left(W_{lm}(\mathbf{r}_0) W_{lm}(\mathbf{r}_0 + \mathbf{r}) \right), \tag{2.22}$$

where $W_{lm}(\mathbf{r}) \equiv \sum_{\alpha=1}^{N_{bond}} w_\alpha Q_{lm}(\mathbf{r}_\alpha)$ is again a sum over all nn bonds of point $\mathbf{r}$. Here w_α are Wigner symbols [40].

2.3.4   Diffusion

Several definitions can be used to calculate the self-diffusion coefficient of particles in the considered system [41]: the diffusion equation, the velocity autocorrelation function and the mean-square displacements of the particles. Analysis of the random Brownian motion of an isolated sphere by the diffusion equation leads to the Stokes-Einstein relation [42] for the self-diffusion coefficient,

$$D = \lim_{\tau \to \infty} \frac{1}{2d\tau} \left\langle \left(\mathbf{r}(t+\tau) - \mathbf{r}(t) \right)^2 \right\rangle. \tag{2.23}$$

Here t is the starting time, $\mathbf{r}$ is the position vector of the particle, d is the dimension of the space, and the brackets denote average over observation time intervals τ for a single particle or over many particles of an ensemble. This relation is obviously valid only if the mean square displacements of particles are asymptotically linear in time. This result can be generalized to that for a diffusion tensor D_{ij}. Another way to determine the self-diffusion coefficient is to use the Green-Kubo formula [43].

2.4   THE LATTICE-BOLTZMANN METHOD

A general statistical mechanics description of fluid motion is given by the Boltzmann equation (BE), without any prior assumptions about *e.g.* hydrodynamical stresses [44]. BE describes the evolution of particle distributions so that its level of description of a given system is somewhere between that of macroscopic hydrodynamics and that of microscopic molecular dynamics. The differential form of BE in the relaxation time approximation is

$$\partial_t f(\mathbf{r}, \mathbf{v}, t) + \mathbf{v} \cdot \nabla f(\mathbf{r}, \mathbf{v}, t) = -\frac{1}{\tau} \left(f(\mathbf{r}, \mathbf{v}, t) - f^{eq}(\mathbf{r}, \mathbf{v}, t) \right), \tag{2.24}$$

where $f(\mathbf{r}, \mathbf{v}, t)$ is the Maxwell-Boltzmann distribution function of a particle at location **r** with velocity **v** at time t, and τ is the relaxation time due to collisions.

The first order solution $O(1/\tau)$ of the BE by using the Chapman-Enskog expansion method gives the Euler equation [45]. This is done by substituting the Maxwell-Boltzmann particle distribution in the steady state and by neglecting the disturbances. The Navier-Stokes equation is a second-order solution $O(\tau^0)$ of BE by

the Chapman-Enskog method [45]. The continuum description of fluid with second order accuracy in space and time is thus given by the continuity and Navier-Stokes (momentum) equations [46],

$$\frac{\partial \rho}{\partial t} + \nabla \cdot (\rho \mathbf{u}) = 0,$$ (2.25)

$$\frac{\partial (\rho \mathbf{u})}{\partial t} + \nabla \cdot (\rho \mathbf{u} \mathbf{u}) = -\nabla p + \nabla \cdot \left[\mu \left(\nabla \mathbf{u} + (\nabla \mathbf{u})^T \right) \right] + \mathbf{F},$$ (2.26)

respectively. Here μ is coefficient of viscosity in the viscous stress term. In the nearly incompressible limit the time derivative of density in Eq. (2.25) is small. The terms on the right hand side of Eq. (2.26) are the induced momentum from the pressure gradient, viscous stress and the external force $\mathbf{F}$.

The key idea behind the LB method [14,47,48,49], is to solve the Boltzmann equation on a regular lattice [11]. At every time step, each 'fluid particle' propagates to a neighbouring lattice point and undergoes local collisions, in which the momenta are redistributed. If the lattice spacing is much smaller than changes in the solid boundaries, *e.g.*, of suspended particles, bulk-like behaviour can be recovered. Fluid particles cannot however be considered as being of microscopic size, they represent a coarse-grained scale which already can support hydrodynamic behaviour, *i.e.*, are of mesoscopic size.

One can rigorously derive the LB method from kinetic theory [50], and there has been significant progress in the development of this method [11, 12 ,51,52]. Quite a lot of benchmarking has been carried out [53,54] in order to show that the LB method to second order accuracy provides a reliable, accurate and efficient algorithm for simulating low Reynolds number incompressible flows with complex boundaries. There are several different lattice-Boltzmann models for incompressible Newtonian fluids [20,55,56,57,58].

The lattice-Boltzmann (LB) method is just one of the methods that are based on solving a discretized form of the Boltzmann equation, other techniques include, *e.g.*, the flux splitting method [59].

2.4.1   LB method for fluid flow

We use here the so-called lattice-BGK [60] (lattice-Bhatnagar-Gross-Krook) algorithm with 9 links per lattice sites (D2Q9) in two dimensions, and with 19 links per lattice sites (D3Q19) in three dimensions [20, 55]. These algorithms have been successfully tested, and the results of several benchmark tests for pure fluid can be found *e.g.* in [III,IV,61,62,63]. The LBGK method is based on the discrete kinetic equation

$$f_i(\mathbf{r} + \mathbf{c}_i, t+1) - f_i(\mathbf{r}, t) = \frac{1}{\tau} \left(f_i^{eq}(\mathbf{r}, t) - f_i(\mathbf{r}, t) \right) + \mathbf{F}.$$ (2.27)

Here $f_i(\mathbf{r}, t) \equiv f_i(\mathbf{r}, \mathbf{v} = \mathbf{c}_i, t)$ is a probability distribution function for 'fluid particles' at link i, $i = 0, ..., N$, moving with discrete speeds $\mathbf{c}_i$ on a lattice $\{\mathbf{r}\}$, τ is the BGK

relaxation parameter, and $f_i^{\text{eq}}(\mathbf{r},t)$ is the local equilibrium distribution towards which the particle populations are relaxed. The set of discrete speeds are chosen such that conservation of mass and momentum as well as Galilean invariance are satisfied. We choose $|\mathbf{c}_0| = 0, |\mathbf{c}_1| = 1, |\mathbf{c}_2| = \sqrt{2}$ for the rest particles, and motions along the nearest neighbour and next-nearest neighbour links, respectively.

A force term $\mathbf{F}$ is included in the LB method to model a pressure gradient needed *e.g.* in channel flow. This body force term adds a constant amount of momentum at every time step on each lattice point, and is equivalent to having a constant body force (or gravity), $\mathbf{F}$, in the Navier-Stokes equation Eq. (2.26) [16].

The LB equation must satisfy mass and momentum conservation, *i.e.*,

$$\sum_{i=1}^{N} C_i(f) = 0,$$
$$\sum_{i=1}^{N} \mathbf{c}_i C_i(f) = 0,$$

(2.28)

where $C_i(f_1,...,f_N) \equiv \dfrac{1}{\tau}\left(f_i^{eq}(\mathbf{r},t) - f_i(\mathbf{r},t)\right)$ is a single relaxation time collision operator in the LBGK method, and represents the change in particle populations due to collisions. Based on kinetic theory, in the equilibrium state where all populations of different particle velocities are in equilibrium, $C_i(f^{eq}) = 0$.

The local equilibrium can be chosen in the form of a quadric expansion of a local Maxwellian distribution [50]:

$$f_i^{\text{eq}}(\mathbf{r},t,\mathbf{u}) = \rho(\mathbf{r},t)\, w_i \left(1 + \frac{\mathbf{c}_i \cdot \mathbf{u}}{c_{\text{s}}^2} + \frac{(\mathbf{c}_i \cdot \mathbf{u})^2}{2c_{\text{s}}^4} - \frac{u^2}{2c_{\text{s}}^2} \right),$$

(2.29)

where the w_i are a set of weight factors which can be chosen such that, *e.g.*, $w_0 = 4/9$, $w_1 = 1/9$, $w_2 = 1/36$ for $D2Q9$, and $w_0 = 1/3$, $w_1 = 1/18$, $w_2 = 1/36$ for $D3Q19$ (see Figure 2.2) [13].
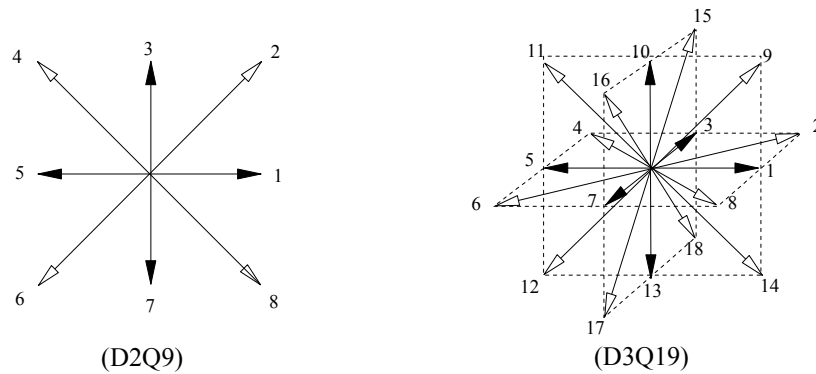

(D2Q9)   (D3Q19)

Figure 2.2 The lattice velocity vectors in the 9-link D2Q9 (left) and 19-link D3Q19 models used in the LB method. The links to nearest neighbours have black arrows and those to next-nearest neighbours have white arrows.

The basic hydrodynamic variables are obtained in the LB method from velocity moments in analogy with the kinetic theory of gases. The density ρ, the flow velocity $\mathbf{u}$ and the 'momentum flux' $\boldsymbol{\Pi}$ of the fluid are given by

$$\rho(\mathbf{r},t) = \sum_{i=1}^{N} f_i(\mathbf{r},t),$$

$$\rho(\mathbf{r},t)\mathbf{u}(\mathbf{r},t) = \sum_{i=1}^{N} \mathbf{c}_i f_i(\mathbf{r},t), \tag{2.30}$$

$$\boldsymbol{\Pi} = \sum_{i=1}^{N} \mathbf{c}_i \mathbf{c}_i f_i(\mathbf{r},t),$$

respectively, where $N = 9$ for $D2Q9$ and $N = 19$ for $D3Q19$.

With these choices Eq. (2.27) can be shown [53] to lead in the continuum limit to the continuity and Navier-Stokes [57,64] equations with sound speed c_s,

$$c_s^2 \mathbf{I} = \frac{1}{d} \sum_{i=1}^{N} w_i \mathbf{c}_i \mathbf{c}_i, \tag{2.31}$$

where d is the dimension of the space. For the $D2Q9$ and $D3Q19$ models we use, Eq. (2.31) gives $c_s = 1/\sqrt{3}$ for the sound speed. The kinematic viscosity of the simulated fluid is given by $\nu = (2\tau - 1)/6$ (in lattice units) [55]. The fluid pressure can be expressed in the form

$$p(\mathbf{r},t) = c_s^2 \Delta\rho(\mathbf{r},t) = c_s^2 \left(\rho(\mathbf{r},t) - \rho_f \right), \tag{2.32}$$

where ρ_f is the average density of the fluid.

Notice that the main collision equation of the LB method is valid only for a low Mach number flow, or in the incompressible limit of the Navier-Stokes equation [65]. This follows from the low-velocity polynomial expansion made to obtain the equilibrium distribution function f^{eq} (see Eq.(2.29)), which approximates the Maxwellian with second order accuracy [66,67].

2.4.2 Surface tension in the LB method

In the LB method surface tension γ results from interaction between fluid particles and is not given as a known macroscopic parameter. It should satisfy Laplace's law, which describes the balance of forces due to pressure difference Δp across an interface, $\gamma = \Delta p \, dV/dA$, with dV and dA small changes in the control volume and area of the interface, respectively. In the case of a spherical droplet with radius R, these changes are $dV = 4\pi R^2 dR$ and $dA = 8\pi R dR$. One thus gets the Laplace law in the form

$$\gamma = \Delta p \, R/2. \tag{2.33}$$

A two-phase LB model was developed by Shan and Chen [68] through a relative forcing scheme,

$$f_i(\mathbf{r}+\mathbf{c}_i,t+1) = f_i(\mathbf{r},t) + \frac{1}{\tau}\left(f_i^{eq}(\mathbf{r},t) - f_i(\mathbf{r},t) \right) + \mathbf{F}_{G,i}(\mathbf{r},t) + \mathbf{F}_{W,i}(\mathbf{r},t), \tag{2.34}$$

where $\mathbf{F}_G$ is the surface tension force and $\mathbf{F}_W$ is the adhesive force at each time step t. The force term $\mathbf{F}_G$ is an attractive short-range force between neighbouring fluid particles [69] of the form $\mathbf{F}_G(\mathbf{r}) = -\tau\psi(\mathbf{r})\sum_i G_i\psi(\mathbf{r}+\mathbf{c}_i)\mathbf{c}_i$, where $\psi(\mathbf{r}) = 1-\exp[-\rho(\mathbf{r})]$ with the total particle density $\rho(\mathbf{r},t)$ defined in Eq. (2.30), and $G_0 = 0, G_1 = 2G, G_2 = G$ (for zero link, nearest neighbour links and next-nearest neighbour links, respectively). Thus a single parameter $G < 0$ controls the surface tension.

Adhesive forces between the fluid and solid phases were introduced via [69] $\mathbf{F}_W(\mathbf{r}) = -\tau\psi(\mathbf{r})\sum_i W_i s(\mathbf{r}+\mathbf{c}_i)\mathbf{c}_i$, where $W_0 = 0, W_1 = 2W, W_2 = W$, and $s = 0,1$ for fluid and solid nodes, respectively. The interaction strength W is positive for a nonwetting and negative for a wetting fluid.

The algorithm can be divided into four major steps. In the first step, the fields at time t, such as the densities and the velocities, are derived. In the second step, the collisions of the total populations are calculated. In the third step, surface tension is introduced and is combined with the total populations. Finally, propagation of the populations is achieved.

2.4.3   LB method for suspension simulations

Several lattice-Boltzmann models for suspensions have already been developed [70,71,72,73]. In order to model the fluid phase in liquid-particle suspensions, we used in Refs. [III,IV] the lattice-Boltzmann model of Ref. [71]. This model was chosen because of computational convenience. It could be efficiently implemented on parallel processors, and all internal and external parameters of the system could easily be varied. All hydrodynamic forces acting on particles and stresses in the fluid phase can also be evaluated without reference to the averaged fluid-dynamical quantities such as the viscous stress tensor [57].

The suspended solid particles obeyed Newtonian dynamics, and their motions were determined by the molecular dynamics method described in Section 2.3.

■ Particle solid boundary nod
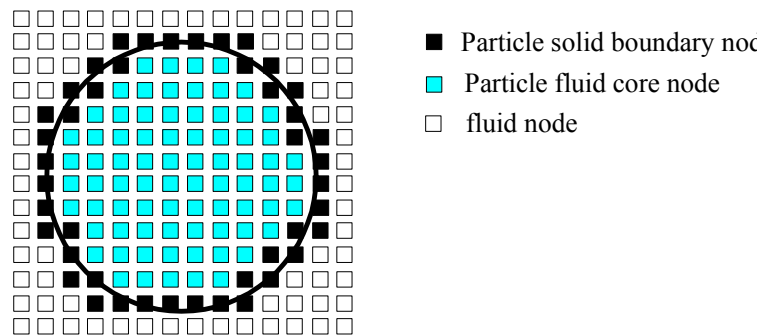□ Particle fluid core node
□ fluid node

Figure 2.3 Schematic picture of a disk particle in a regular lattice with solid, internal and external fluid boundary nodes.

In the model used here, a solid particle consists of a solid matrix, and of an interior fluid that is called the fluid core of the particle. There are two kinds of lattice points inside a particle, the interior points and the boundary points. Each boundary point has at least one link pointing to the fluid phase. The lattice-Boltzmann collision operation (Eq. (2.27)) is applied at every lattice node including the boundary and interior points of the particles.

The no-slip boundary condition at solid-fluid interfaces is usually realised in lattice-Boltzmann simulations through a simple bounce-back condition, where the momenta of the fluid particles are reversed at the boundary points [70, 71]. The bounce-back condition can be generalised to moving boundaries, whereby the particle distributions are modified at boundary points such that [70, 71]

$$f_i(\mathbf{r}+\mathbf{c}_i,t+1) = f_{i'}(\mathbf{r}+\mathbf{c}_i,t_+) + 2\rho_f B_i(\mathbf{u}_w \cdot \mathbf{c}_i). \tag{2.35}$$

Here t_+ indicates the time right after the collision and i' denotes the bounce-back link. Also, coefficients $B_0 = 0, B_1 = 1/3$ and $B_2 = 1/12$ apply for $D2Q9$ in two-dimensions, and $B_0 = 0, B_1 = 1/6$ and $B_2 = 1/12$ for $D3Q19$ in three-dimensions, for the rest particles, and motions along the nearest neighbour and next-nearest neighbour links, respectively. Finally $\mathbf{u}_w$ is the wall velocity at point $\mathbf{r}_w$. It is determined by the particle center of mass position $\mathbf{r}_c$ and velocity $\mathbf{U}$, and angular velocity $\boldsymbol{\omega}$, such that

$$\mathbf{u}_w = \mathbf{U} + (\mathbf{r}_w - \mathbf{r}_c) \times \boldsymbol{\omega}. \tag{2.36}$$

The last term in Eq. (2.35) accounts for the momentum transfer between the fluid and the moving solid wall. Note that Eq. (2.35) is also used to implement the moving solid boundary walls in Couette flow with $\mathbf{u}_w$ the channel wall velocity.

The forces and torques on a solid particle are calculated as sums of momentum changes over the particle surface nodes,

$$\mathbf{F}_p(t) = \sum_s \Delta\rho_f \mathbf{u}_w,$$
$$\mathbf{T}_p(t) = \sum_s \mathbf{r}_w \times \Delta\rho_f \mathbf{u}_w. \tag{2.37}$$

The mass M_s of a solid matrix is uniformly distributed in the interior and boundary points giving it an effective density ρ_s. However, the solid matrix interacts with the fluid phase and with the core fluid only at the boundary points. The total hydrodynamic force and torque acting on the solid matrix can be obtained at each time step by summing the effect of Eq. (2.35) at all boundary points. The solid matrix can then be moved according to normal Newtonian dynamics with particle properties such as location, velocity, angular velocity, force and torque.

2.4.4   Momentum transfer in suspensions

When analysing the rheological behaviour of particle suspensions, it is important to understand the underlying mesoscopic mechanisms that contribute to the total

observable shear stress (and apparent viscosity). To this end we need to calculate the stresses of different phases and momentum fluxes.

The fluid momentum tensor $\mathbf{\Pi}_f$ can be obtained from the LB pre-collision and post-collision populations f_i and f_i^* (Eq. (2.34)) such that

$$\Pi_f^{\alpha\beta}(\mathbf{r},t) = \frac{1}{2}\sum_{i=1}^N c_{i\alpha}c_{i\beta}f_i(\mathbf{r},t) + \frac{1}{2}\sum_{i=1}^N c_{i\alpha}c_{i\beta}f_i^*(\mathbf{r},t), \tag{2.38}$$

where α, β denote the spatial components of tensor $\mathbf{\Pi}_f$.

The convection tensor for each solid or fluid phase $(v = s, f)$,

$$\mathbf{C}_v = \rho_v \mathbf{u}\mathbf{u}, \tag{2.39}$$

can be directly calculated from density ρ_f and velocity (of the node) $\mathbf{u}$ (Eq. (2.30)), and the viscous stress tensor $\mathbf{\Sigma}_f$ is given by

$$\mathbf{\Sigma}_f = \mathbf{\Pi}_f - \mathbf{C}_f. \tag{2.40}$$

The total momentum flux $\mathbf{F}$ through any surface S which intersects the system is given by

$$\mathbf{F} = \int_S \mathbf{\Pi} \cdot d\mathbf{S}, \tag{2.41}$$

where $\mathbf{\Pi}$ is the total momentum tensor. In the present case it can be written as

$$\mathbf{\Pi} = \mathbf{C}_f + \mathbf{C}_s + \mathbf{\Sigma}_f + \mathbf{\Sigma}_s, \tag{2.42}$$

where $\mathbf{C}_f$ and $\mathbf{C}_s$ are the convective momentum tensors, and $\mathbf{\Sigma}_f$ and $\mathbf{\Sigma}_s$ are the internal stress tensors for the fluid and the solid phase, respectively. A schematic illustration of the simulation setup together with a snapshot of an actual solution for the Couette flow of the suspension is shown later in Figure 6.1. In this figure the surface $S = S(y)$ is a plane perpendicular to the y axis. The total shear stress acting on this plane is defined by

$$\tau_T = \mathbf{\sigma}_f + \mathbf{\sigma}_s + \mathbf{\tau}_f + \mathbf{\tau}_s \equiv \left\langle \mathbf{C}_f^{xy} \right\rangle + \left\langle \mathbf{C}_s^{xy} \right\rangle + \left\langle \mathbf{\Sigma}_f^{xy} \right\rangle + \left\langle \mathbf{\Sigma}_s^{xy} \right\rangle, \tag{2.43}$$

where $\langle \ \rangle$ denotes averaging over space, time and ensemble. Here we calculate all averaged quantities in a macroscopically stationary state and, assuming ergodicity, perform averaging over a long period of time, over volume or surface, and over a number of macroscopically identical systems. Stresses $\mathbf{\sigma}_f$ and $\mathbf{\sigma}_s$ contain the stresses due to pseudo-turbulent motion of the two phases, $\mathbf{\tau}_f$ contains the viscous stress of the fluid phase and $\mathbf{\tau}_s$ contains the internal stress of particles (and corresponds to the elastic stress of physical solid particles).

Stresses $\mathbf{\sigma}_f$, $\mathbf{\tau}_f$ and $\mathbf{\sigma}_s$ can all be directly calculated for each lattice point using Eqs. (2.38)-(2.40). Notice that in $\mathbf{\sigma}_s$ both the convection of the solid matrix and the convection of the fluid core have to be included. Notice also that the convection and stress of fluid at the boundary points of the particles are included in $\mathbf{\sigma}_f$ and $\mathbf{\tau}_f$, respectively.

Evaluation of the actual stress distribution inside solid particles would require solving, separately for each suspended particle, time-dependent elastic continuum

equations with boundary conditions given by the hydrodynamic forces due to the surrounding fluid, and the impulsive forces due to particle-particle collisions. Fortunately, it is not necessary to carry out here this formidable numerical effort. The stress $\boldsymbol{\tau}_s$ can be written in the form

$$\boldsymbol{\tau}_s = \boldsymbol{\tau}_c + \boldsymbol{\tau}_{pp} + \boldsymbol{\tau}_{fp}, \tag{2.44}$$

where $\boldsymbol{\tau}_c$ is the stress in the core fluid while $\boldsymbol{\tau}_{pp}$ and $\boldsymbol{\tau}_{fp}$ are the stresses in the solid matrix caused by particle-particle collisions and by interactions between the fluid and the particle, respectively. The stress $\boldsymbol{\tau}_c$ can be obtained directly from Eq. (2.40). In order to calculate stresses $\boldsymbol{\tau}_{pp}$ and $\boldsymbol{\tau}_{fp}$, we consider an impulsive force $\mathbf{F}_{pp}$ due to particle-particle collisions, and a force $\mathbf{F}_{fp}$ due to the hydrodynamic interactions that also acts on a surface A_p formed by the intersection of surface S with the particle (see the insets in Figure 6.1). Since the collisions are assumed frictionless, and the particles are circular and smooth, the angular velocity does not change in a collision. It is then easy to show that the collisional force on A_p can be written as

$$\mathbf{F}_{pp} = \frac{m_d \Delta \mathbf{p}}{M_s \Delta t}, \tag{2.45}$$

where Δt is the collision time (1 in lattice units), M_s is the total mass of the solid matrix of the particle, m_d is the mass of the lower part of the particle, and $\Delta \mathbf{p}$ is the total momentum change of the particle due to collision (see inset (b) in Figure 6.1). In simulations, mass m_d can simply be calculated by counting the number of lattice points that are located below the plane S inside the particle.

While deriving the force $\mathbf{F}_{fp}$, the effect of fluid phase and fluid core on the solid matrix must both be included. The equation of motion for the lower part of the particle, as shown in inset (a) of Figure 6.1, gives

$$\mathbf{F}_{fp} = -\mathbf{F}_{i,d} - \mathbf{F}_{o,d} + m_d \mathbf{a} + m_d \boldsymbol{\alpha} \times \mathbf{r}_d + m_d \boldsymbol{\omega}^2 r_d \mathbf{e}_y. \tag{2.46}$$

Here $\mathbf{F}_{i,d}$ and $\mathbf{F}_{o,d}$ are the hydrodynamic forces due to the fluid core and the fluid phase out of the core on the solid matrix (which can be obtained from Eq.(2.37)), m_d is the mass of the lower part of the particle, and $\mathbf{a}$, $\boldsymbol{\alpha}$ and $\boldsymbol{\omega}$ are the acceleration, angular acceleration and angular velocity of the whole solid matrix, respectively. Finally, $\mathbf{r}_d$ is a vector pointing from the center of the particle to the center-of-mass of the lower part of the particle. The contribution of collisions and hydrodynamic interactions to the total shear stress is now given by $\tau_{pp} = \left\langle F_{pp}^x / A_p \right\rangle$ and $\tau_{fp} = \left\langle F_{fp}^x / A_p \right\rangle$.

More details of the lattice-Boltzmann suspension code we use, together with benchmark results, are given in Refs. [III,IV].

3 MD SIMULATIONS OF A GRANULAR MEDIUM

3.1 INTRODUCTION

Even though fluids can be adequately modelled on the mesoscopic or macroscopic scale using the Navier-Stokes equations, it is nevertheless interesting to study microscopic scale phenomena like diffusion and phase transitions. Many natural phenomena like avalanches, landslides, and soil fluidisation, can be related to granular flows that involve diffusion processes. Broadly speaking the individual molecules of a fluid build up a granular medium through interparticle 'contacts' [74,75,76].

In these systems mixing is an important phenomenon which occurs due to the diffusive motion of the particles. This diffusion has been analyzed by kinetic theory of rapid granular flows [77,78], laboratory experiments [79,80] and numerical simulations [81,82,83].

In Campbell's [82] review of results prior to 1990 concerning diffusion in molecular dynamics simulations of dense granular media, lack of diffusion for solid volume fractions over 0.56 is reported. This means that diffusive motion of particles may be suppressed by high densities. Campbell's conclusion was based on a series of computer simulations for unbounded granular shear flows. Such lack of diffusion was, however, not observed in later computer simulations on bounded rapid granular flows [84]. Hence, it was important to further examine this issue, and we studied it by simulating a Couette flow of inelastic, rough, hard spheres.

Our simulations were carried out in a cell under periodic boundary conditions in the y and x directions, with a velocity gradient imposed in the z direction. Two massive walls, with the same properties as the interior particles, were fixed to move in opposite directions parallel to the x direction (see Figure 3.1).
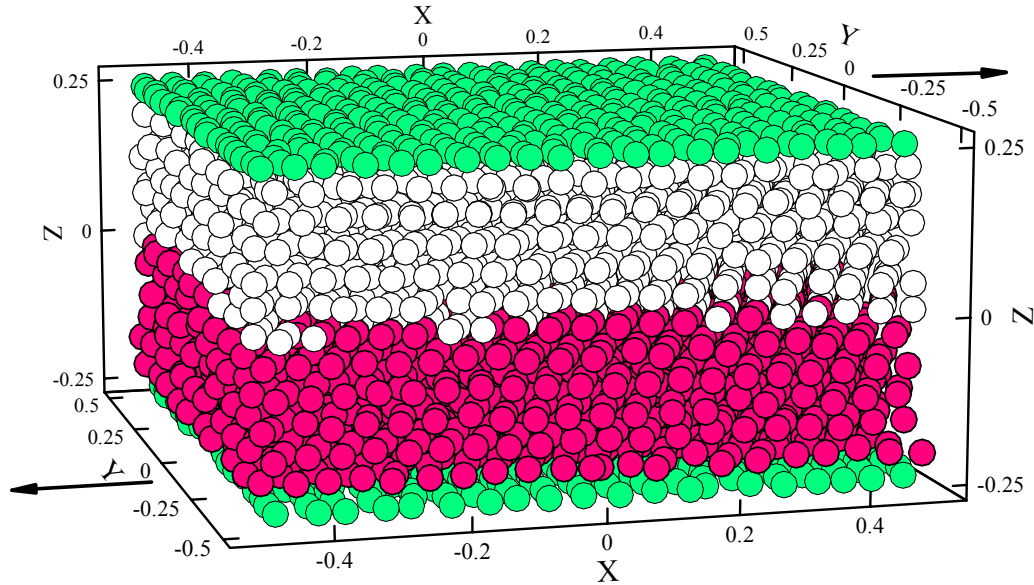
Figure 3.1 A schematic picture of the initial configuration of dark and light particles in the computational box which includes the wall particles.

The number of particles in the interior and in the walls varied from 4296 to 4824, and from 400 to 625, respectively. This meant that for concentration ranged from 0.5 to 0.6. All the simulations began with an initial set of random overlapping spheres using the method of Ref. [85]. Then the individual spheres were moved randomly until the overlaps were removed. On one side of the plane $Z = 0$ the particles were marked dark, whereas on the other side the particles were marked white (see Figure 3.1).

Granular shear flow with average shear rate from zero to $\gamma_w = 2u_w/H \approx 4\,s^{-1}$ was then studied using the molecular dynamics method (see chapter 2): $\mathbf{u}_w$ is the wall velocity and H is the gap between the walls. The particles were modelled as inelastic, rough, hard spheres with radius R for which $H/2R \approx 10$. In order to simulate a dense granular flow, Lun and Bent [86] suggested certain values for the dissipation parameters. Using their values (*i.e.*, the coefficient of restitution $e = 0.93$, the surface friction coefficient $\mu = 0.123$, and the phenomenological constant for sticking contacts $\beta_0 = 0.4$), the collision frequency was 600 kHz, which was close to the value reported previously [80].

3.2   RESULTS AND DISCUSSION

From the simulations, stress fluctuations, diffusion coefficient tensors, velocity distributions, density profiles, radial distribution functions, and correlation functions were determined.
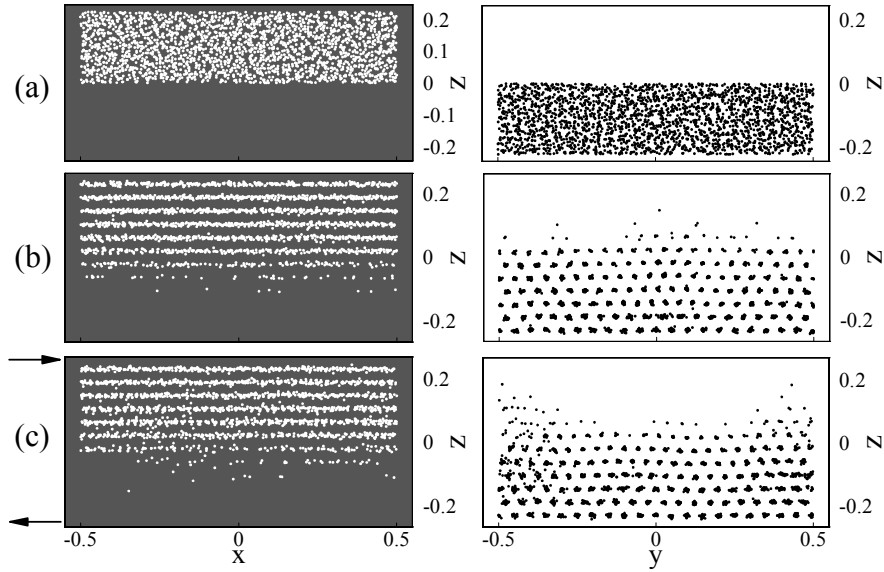
Figure 3.2 Snapshots of **(a)** the initial configuration of white and black particles, and at **(b)** $t^* = 59$ and **(c)** $t^* = 250$, projected to the xz (left) and yz planes (right). The arrows indicate the shear flow direction.

Snapshots of a system with solid volume fraction $\phi = 0.565$ and shear rate $\gamma_w \simeq 4\,s^{-1}$ are shown in Figure 3.2. The snapshots are projections of particle locations to planes parallel and normal to the shear flow, respectively. From Figures 3.2 (b) and (c) a 'diffusive' evolution of the system can be seen. This is in contrast with what Campbell [82] reported on the absence of diffusion. The lack of self-diffusion may have been induced by an ordered initial configuration in their simulations. The ordered layers in the xz plane from a close to hexagonal pattern in the yz plane (the pattern is also close to icosahedral).
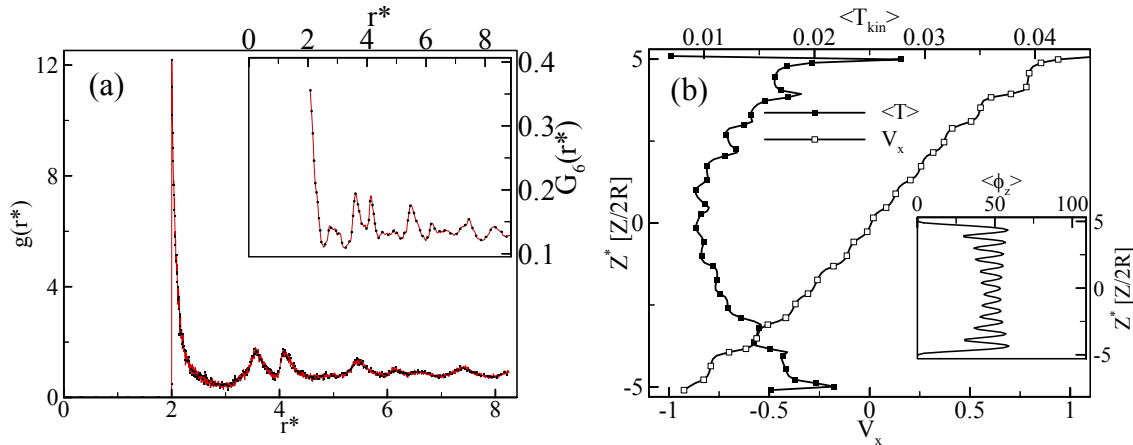

Figure 3.3 **(a)** Radial distribution function in the equilibrium situation ($\phi = 0.56, \gamma_w = 4\,s^{-1}, t^* \approx 250$) as a function of dimensionless radial distance $r^* = r/R$. **(b)** Velocity profile and kinetic granular temperature at $t^* = 150$, with $\phi \sim 0.5$ and $\gamma_w = 4\,s^{-1}$, as functions of dimensionless channel height ($Z^* = Z/2R$). The inset shows the average density profile across the sample.

The radial distribution function shown in Figure 3.3a has a peak at $r^* = r/R \approx 2\sqrt{3}$, indicating localised ordering around the particles. This means that the initially disordered system has evolved to an ordered state in the presence of shear flow. The degree of translational order $(\rho_\mathbf{k})$ was tested according to Eq. (2.20) by choosing $\mathbf{k} = (2\pi/l)\mathbf{z}$, where $\mathbf{z}$ is a unit vector in the z direction.

We found that is 0.8 for $l \approx H/11$ (see also Figure 3.3b). This could indicate a layered state with eleven layers. We also found that $\rho_\mathbf{k} \approx 0$ in the direction $(-\mathbf{x}, +\mathbf{y}, -\mathbf{z})$, thus verifying the absence of cubic symmetry (the sliding fcc phase). We investigated therefore a set of orientational order parameters, denoted by $\bar{Q}_{lm}(\mathbf{r})$ as described in Eq.(2.21) and Table 2.1, associated with each bond with 12 nearest neighbours. Nonzero value of this order parameter indicates an ordered structure.

We found that $Q_6 \approx 0.4$ suggesting an icosahedral lattice. However, the value $Q_8 \approx 0.24$ suggested that the symmetry of the bond-oriented states is not perfectly icosahedral and, as can be seen from the final configuration in Figure 3.2, the structure is rather close to that of a simple hexagonal lattice. More information regarding possible types of orientational order of the above-mentioned system can be obtained from the bond-angle correlation functions $\bar{G}_l$ (see Eq. (2.22)) [39]. The value of $\bar{G}_6(r^*)$ at large r^*, shown in the inset of Figure 3.3a, also indicates that the system is close to an icosahedrally oriented liquid, possessing a degree of symmetry intermediate between those of a crystal and a liquid. In conclusion, for a high average shear rate, the system of inelastic, rough, hard spheres displays the symmetry of imperfect icosahedral or hexagonal liquid for solid volume fractions larger than $\phi = 0.565$.

In d dimensions, the average translational kinetic energy of particles whose velocities satisfy the Maxwell-Boltzmann distribution, is $< \frac{1}{2} \sum_{i=1}^{N} m_i u_i^2 > = \frac{d}{2}kT$. The kinetic granular temperature T_{kin} is given by

$$T_{kin} \equiv \frac{1}{d}\sum_{k=1}^{d} \frac{\sum_{i=1}^{N_k} \rho_{i,k}\left[(\mathbf{u}_i - \bar{\mathbf{u}}_k)\cdot(\mathbf{u}_i - \bar{\mathbf{u}}_k)\right]}{\sum_{i=1}^{N_k} \rho_{i,k}}, \qquad (3.1)$$

where $\rho_{i,k}$ is the volume of slice k covered by particle i, and $\mathbf{u}_i$ is the particle velocity with the average $\bar{\mathbf{u}}_k \equiv \sum_{i=1}^{N_k} \rho_{i,k}\mathbf{u}_i \left/ \sum_{i=1}^{N_k} \rho_{i,k}\right.$.

In Figure 3.3b we show the velocity and density profiles, and the local kinetic granular temperature. A layered structure in the yz plane is evident from the density profile, and an S-shaped velocity profile and a high granular temperature near the walls can also be observed. We found that the granular temperature is

proportional to the transverse self-diffusion coefficient, $D^* \propto \sqrt{T}$, which can be understood from dimensional analysis (Eq. (2.23)).

The amplitude fluctuations of the dimensionless normal stress on the walls ($P^*\left(t^*\right) = P/\left[\rho_p\, 4R^2\gamma_w^2\right]$ with $t^* = t\, u_w/H$ the dimensionless time and ρ_p the particle density [87]), was found to obey a strongly asymmetric distribution similar to those observed in recent experiments [79]. For a system with $\phi = 0.565$ and $\gamma_w = 4\, s^{-1}$ at $t^* \approx 200$, the amplitude of stress fluctuations on the wall increased with increasing coefficient of restitution (from $e = 0.84$ to $e = 0.93$), and decreased with surface friction (from $\mu = 0.41$ down to $\mu = 0.123$) as shown in Figure 3.4a. For $e = 0.84$ and $\mu = 0.41$ at $t^* > 200$, the fluctuations were much smaller than those observed by Savage and Sayed [87]. In the opposite case, by increasing the coefficient of restitution to $e = 0.93$, and decreasing the surface friction coefficient to $\mu = 0.123$, the result was closer to those in the annular shear cell tests of Ref. [87]. However, all the results obtained were much smaller than those for gravity-driven channel flows [79].

The decay of the absolute value of the mean dimensionless normal stress, $\left|P^*\right|$, appears to be almost exponential before $t^* \approx 200$, as evidenced by Figure 3.4a. There is, however, an additional decrease of $\left|P^*\right|$ at about $t^* \approx 200$ ($\sim 5\times10^7$ collisions), which might indicate a phase transition. Other evidence for a transition could be obtained from translational and bond orientational parameters [I, 87], and from the radial distribution function.

The stress fluctuations on the walls increased with the solid volume fraction when the latter was increased from 0.56 to 0.58 (c.f. Figure 3.4a). Meanwhile the self-diffusion coefficient (measured from the slope of the mean square displacement curve for dimensionless time intervals $\tau^* > 1$), decayed further approaching a value close to those of recent experimental observations [79, 83]. The increased stress fluctuations may be the result of higher dissipation at 0.58 leading to the decrease in the transverse self-diffusion coefficients. At $\phi = 0.582$, diffusion decays rapidly with time (at $t^* = 245$) to $D^* \approx 10^{-5}$ (the diamonds in Figure 3.4b). This also is an evidence of a phase transition to an ordered state or to a structural arrest. In an ordered system fluctuations induced changes in the geometry of the cage formed by the nearest neighbours around a particle become infrequent. This could result in a dramatic decay of the long-time transverse self-diffusion coefficient.
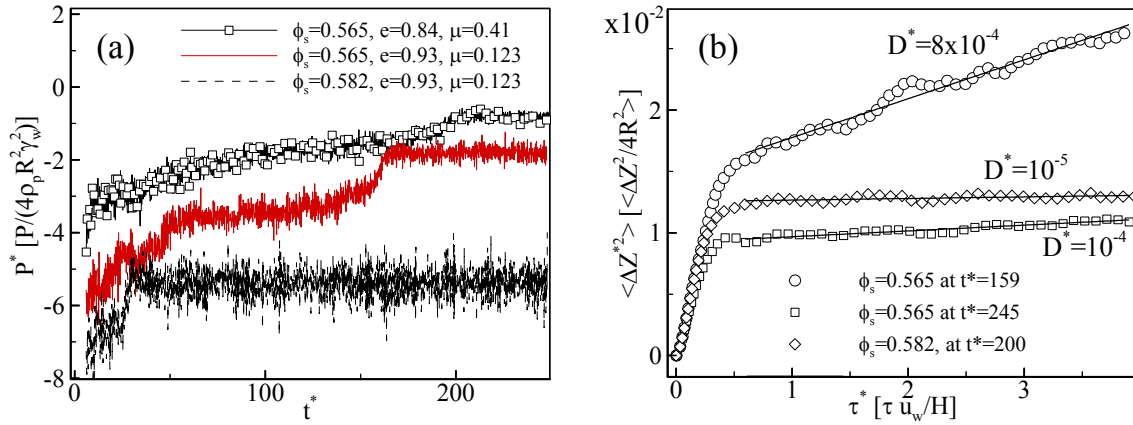
Figure 3.4 **(a)** Dimensionless normal stress, exerted by the particles on the bottom wall as a function of dimensionless time t^*, for three indicated sets of parameters. **(b)** Dimensionless mean square transverse displacement $<\Delta Z^{*2}>$ as a function of dimensionless time τ^*, for three sets of parameters that include the starting time of the analysis t^*. Solid lines are linear fits to the data for $\tau^* > 1$.

Also shown in Figure 3.4b are the self-diffusion coefficients for the cases $\phi = 0.565, t^* = 159, 245$. The coefficients decay from $\sim 10^{-3}$ up to 10^{-4} when t^* increases from 159 to 245. This is consistent with the result presented in Figure 3.4a. In order to test that the behaviour we found above for rough particles is not due to roughness only, we did some of the analyses for systems of smooth particles. For a solid volume fraction of 0.565 and a sufficiently long starting time of $t^* \approx 40$, our results show that the calculated dimensionless long-time transverse self-diffusion coefficient for the system comprised of smooth particles is $D^* = 1.2 \times 10^{-2}$, which is an order of magnitude higher than that for the system of rough particles $D^* = 1.5 \times 10^{-3}$ (not shown). The above-mentioned value for the system of smooth particles is close to those reported in Ref. [79] for moderate shear rates. It appears that shearing of particles with rough surfaces generates lower normal stress than a similar shearing of smooth particles. This may be interpreted such that rough particles tend to have more rotational energy than smooth particles. Moreover, particles with rough surfaces lack transverse diffusional movements. This observation supports the Menon and Durian results [80] in that the dynamics of grains in a dense granular flow are dominated by collisions rather than sliding contacts.

A comparison between diffusion coefficients for different volume fractions in granular media revealed that for dilute systems, the velocity autocorrelation function also decays exponentially as predicted by kinetic theory [88]. Results are shown in Figure 3.5 for a dilute and a dense system. For the higher volume fraction, $\phi \sim 0.51$, the velocity autocorrelation decays faster, and correspondingly there is a smaller diffusion coefficient.
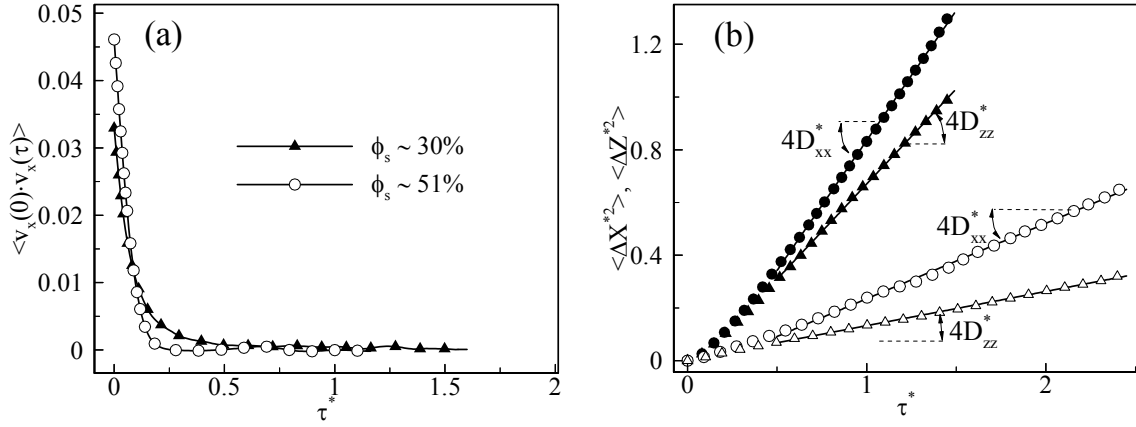
Figure 3.5 **(a)** Velocity autocorrelation function as a function of dimensionless time for $\phi \sim 30\%$ (black symbols) and $\phi \sim 51\%$ (white symbols). **(b)** Dimensionless mean square transverse displacements $<\Delta Z^{*2}>$ of a system of smooth particles as a function of dimensionless time τ^*. Solid lines are linear fits to the data. Filled symbols denote 30% solid volume fraction and white symbols 51% solid volume fraction.

Our results also show that in the stream direction the self-diffusion coefficient was much higher than in the transverse directions for both smooth and rough particles, in agreement with the experimental results of Hsiau and Shieh [89].

In conclusion, our numerical simulations of a sheared, dense, monosized granular material indicate there is a phase transition at long run times for systems of rough particles, which causes a sharp drop in the dimensionless transverse long-time self-diffusion coefficient of the particles. However, the system is diffusive at solid volume factions even higher than 0.56. The structure of the ordered state was found to be closer to that of a simple hexagonal lattice rather than icosahedrally oriented liquid. A similar behaviour could be seen in system of smooth particles so that the self-diffusion coefficient decreased by increasing concentration. In this case, the self-diffusion coefficient was much higher in the stream direction than in the transverse directions, and much smaller than that for rough particles.

4   CAPILLARY RISE

In this section we review our results for simulations on single- and two-phase fluids. The purpose of these simulations was to better understand the solid-liquid (wetting) and gas-liquid (surface tension) interactions. It would also be interesting to see how well the LB method is capable of simulating the well-known capillary rise phenomenon, and the method was thus tested on an uprising fluid in a narrow capillary pipe [II].

4.1   THE HYDRODYNAMICS OF CAPILLARY RISE

The capillary rise phenomenon has been of wide theoretical and practical interest in the recent years [90,91,92,93,94], with applications ranging from simple capillary rise and imbibition (penetration of liquid (droplet) into a porous material) to droplet spreading and other phenomena related to wetting. The basic analytical theories for capillary rise were developed a long time ago [95], but recent experimental and numerical techniques have provided new insight into this problem: on the numerical side first the LGA models [16, 14 ,96,97,98] and then the more recent LB method [II, 55 , 96 ,99].

In the classical analysis by Washburn [100], the motion of an incompressible fluid is treated as a Poiseuille flow [101]. When we consider the rise of an incompressible liquid in a capillary pipe, we can thus start from the Hagen-Poiseuille equation for a fully developed pipe flow under a pressure drop of ΔP,

$$\frac{\mathrm{d}Q}{\mathrm{d}t} = \frac{\pi \Delta P r^4}{8\mu_f \left(h + h_+\right)},\tag{4.1}$$

where $\mathrm{d}Q/\mathrm{d}t = \pi r^2\,\mathrm{d}h/\mathrm{d}t$ is the volumetric flow rate, h is the height of the rising liquid column from the level of the liquid surface outside the pipe, h_+ is the length of the capillary pipe immersed in the liquid, r is the radius of the pipe, and is μ_f the viscosity of the liquid. The total pressure drop may be expressed as a sum of capillary pressure and the static pressure exerted by gravity:

$$\Delta P = \frac{2\gamma \cos\theta_d}{r} - \rho_f gh,\tag{4.2}$$

where fluid density, surface tension and dynamic contact angle are denoted by ρ_f, γ and θ_d, respectively.

In the classical capillary rise theory the contact angle is constant, but in the phenomenologically corrected version [100] of this theory contact angle varies with velocity, and is thus called the dynamic contact angle. Combining Eqs. (4.1) and (4.2) one can write

$$8\mu_f(h+h_+)\frac{\mathrm{d}h}{\mathrm{d}t} = 2r\gamma\cos\theta_d - r^2\rho_f gh. \tag{4.3}$$

By including inertial and entrance effects [101], and by rearranging the terms, Eq. (4.3) becomes

$$\cos\theta_d = \frac{1}{2\gamma}\left(\rho_f rh\frac{\mathrm{d}^2h}{\mathrm{d}t^2} + \frac{8\mu_f(h+h_+)}{r}\frac{\mathrm{d}h}{\mathrm{d}t} + \frac{1}{4}\rho_f r(\frac{\mathrm{d}h}{\mathrm{d}t})^2 + \rho_f rgh\right). \tag{4.4}$$

This is the Washburn equation whose solution we will use to compare with the simulated column height, with the dynamical contact angle first determined by simulations.

Inertial forces can usually be ignored in the overdamped limit $r < r_c = \left(32\mu_f^2\gamma\cos\theta_d / \rho_f^3 g^2\right)^{1/5}$ [102], which condition is satisfied by the parameter values in our system. Asymptotically and at long times $(t \to \infty)$, when $\mathrm{d}h/\mathrm{d}t \to 0$, one finds that

$$h_\infty = \frac{2\gamma\cos\theta_\infty}{\rho_f gr}, \tag{4.5}$$

where $\theta_\infty = \lim_{t\to\infty}\theta_d$. Due to the rough discretization and the steep density variation especially for small r, it is difficult to accurately measure θ_d directly from the simulated density field. For an indirect determination of θ_d, we first apply the one-dimensional Reynolds transport theorem in a control volume to estimate the rate of change of the momentum of the system. The upper control surface moves with the meniscus of the liquid column (no outflow from the control volume) and the lower control surface is fixed at the lower end of the pipe. Then the rate of change of the total momentum inside the control volume is

$$\frac{\mathrm{d}}{\mathrm{d}t}(m\mathbf{v})_{\mathrm{syst}} = \frac{\mathrm{d}}{\mathrm{d}t}[\int_{CV}\mathbf{v}\rho\mathrm{d}V] + \int_{CS}\mathbf{v}\rho(\mathbf{v}\cdot\mathbf{n})\mathrm{d}A, \tag{4.6}$$

where $m = m(t)$ is the total mass of the fluid inside the control volume, $\mathbf{v}$ is the fluid velocity, and CV and CS denote the volume and the surface area of the control volume, respectively. By integration we find that

$$\frac{\mathrm{d}}{\mathrm{d}t}[\int_{CV}\mathbf{v}\rho_f\mathrm{d}V] = \rho_f\pi r^2\left(h\frac{\mathrm{d}\mathbf{v}}{\mathrm{d}t} + \mathbf{v}\frac{\mathrm{d}h}{\mathrm{d}t}\right) = \frac{\mathrm{d}(m\mathbf{v})_{cv}}{\mathrm{d}t},$$
$$\int_{CS}\mathbf{v}\rho(\mathbf{v}\cdot\mathbf{n})\mathrm{d}A = -\mathbf{v}(\rho_f\pi r^2 v). \tag{4.7}$$

where **v** and **n** are liquid velocity and a unit vector normal to the inlet control surface, respectively. Assuming a constant velocity through the control surface, we obtain an expression for θ_d by substituting Eq. (4.4) into Eqs. (4.6) and (4.7),

$$\cos\theta_d = \frac{1}{2\pi r\gamma}[\frac{\mathrm{d}(mv)_{cv}}{\mathrm{d}t} - \frac{3}{4}\rho_f\pi r^2 v^2 + 8\pi\mu_f(h+h_+)v + \rho_f\pi r^2 gh]. \qquad (4.8)$$

This equation can be used to determine θ_d from the simulated $h(t)$. Notice that this is the correct form for Eq. (8) in Ref. [II]. However, the results remain almost unchanged, especially at long times, because the rise velocity is very small.

The height of the column $h(t)$, or the location of the gas-liquid interface, was determined as the turning point of a least-squares fit by a tanh function of the density profile in the vertical direction.

A number of empirical relationships for wetting have been discussed in the literature, all of which express the dynamic contact angle θ_d as a function of the capillary number $\mathrm{Ca} = v\mu/\gamma$ during spreading such that $\theta_d = f(\mathrm{Ca}, \theta_a)$, where the advancing contact angle θ_a is that of a spreading liquid in the limit $v \to 0^+$. We adopted the expression generally used in studies of capillary rise [102],

$$\cos\theta_d = \cos\theta_a - A\mathrm{Ca}^B, \qquad (4.9)$$

where A and B are constants. This dependence on θ_a and Ca of θ_d was tested by simulations, and a reasonable agreement was found.

4.2   RESULTS AND DISCUSSION

We first simulated a three-dimensional two-phase fluid system by using the LB method [II] with periodic boundaries in the lateral directions and without any pipe. The simulation code has already been tested for single-phase fluid and flow through porous media, and many benchmark results have been reported [62]. After a certain number of iterations, when the system reached the equilibrium state, the pipe was inserted, and the simulation was continued until saturation of the capillary rise (c.f. the snapshots in the insets of Figures 4.3 and 4.4 for r=5 and 20, respectively).

The simulations reported below were performed for pipe radii $r = 2, 5, 10$, while the full domain size was $50 \times 50 \times 200$, and $100 \times 100 \times 300$ for $r = 20$. In all capillary rise simulations the relaxation parameter was $\tau = 1$, and unless stated otherwise, the adhesive parameters were $W = -0.1$ and $G = -0.15$. This resulted in $\rho_f/\rho_g \approx 20$, with the bulk density of the liquid phase $\rho_f = 2.25$, viscosity $\mu_f = 0.375$, and the surface tension $\gamma = 0.085$.

Dimensional analysis for the group of variables $(h, t, g, \rho_f, \mu_f, \gamma)$ was done for presenting the results in dimensionless units. We thus defined the characteristic time, velocity and height as $t_0 = \mu_f^3/\rho_f\gamma^2 \approx 3.2$, $v_0 = \gamma/\mu_f \approx 0.23$ and $h_0 = \mu_f^2/\rho_f\gamma \approx 0.74$, respectively. In the presence of gravity, we also used the dimensionless parameter $\tilde{g} = \mu_f^4 g/\rho_f\gamma^3$.

An important issue is whether variation in the capillary radius changes the dynamics of the flow in the two-phase flow model. To address this question we calculated the velocity profile for pipes with different radii, and compared them with the analytical results [101] (see Figure 4.1). This velocity profile could be determined from a steady flow of the single- or two-phase fluid at its equilibrium density between two infinite (periodic boundary conditions in the lateral directions) parallel plates. A constant body force at each lattice point produced the flow without any phase separation in the two-phase model. The well-known analytical results for Poiseuille flow [101] are also shown in Figure 4.1 by the full lines.
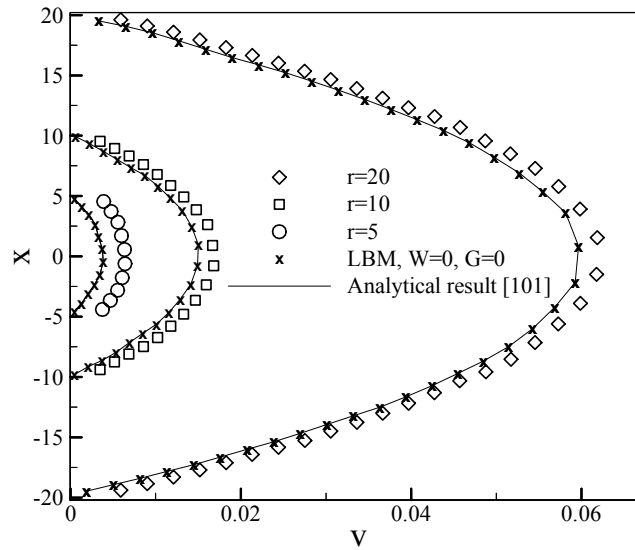
Figure 4.1 A typical example of the velocity profile of the fully developed flow of a single-phase ($W = G = g = 0$) fluid, and of a two-phase ($W = -0.1$, $G = -0.15$, $g = 0$) fluid, between two parallel plates.

A comparison with analytical results showed that in our simulations the velocity profile had the correct (Poiseuille) parabolic form but it was shifted forward. This relative deviation increased for decreasing r as expected from the boundary effects. The reason for this deviation was a strong boundary-layer effect. The adhesive force $\mathbf{F}_G$ defined in Eq. (2.34), generates a low-density liquid layer on the pipe surface. Due to very low resolution, we did not expect sensible results for $r = 2$, and for strong adhesion also $r = 5$ and $r = 10$ were too small. As seen in the density profiles of Figure 4.2, the narrow pipe with radius $r = 2$ did not have the bulk liquid density anywhere in the pipe. The decay of density close to the inside walls of the pipe was however similar for all $r = 5, 10, 20$, at least for weak adhesion forces, *e.g.* $W = -0.1$ (see Figure 4.2). The proportion of the liquid with bulk density decreased with decreasing radius.

For increasing adhesion we observed that the simulated velocity profile approached the theoretical curve, and that the boundary effects decreased in the density profile (see the curves for $r = 20$ in Figure 4.2). At the same time, due to increased discrete-

lattice effects at the gas-solid interface, values for $\cos\theta_d$ greater than unity were obtained for small r, which is clearly unphysical.
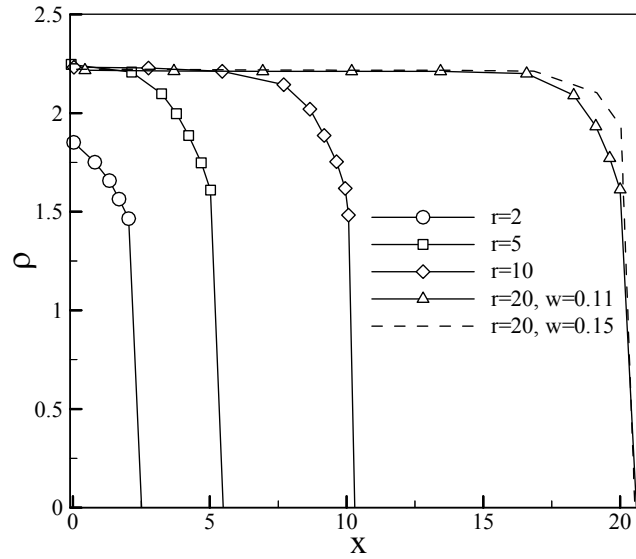

Figure 4.2 The density profiles across the capillary pipe for radii $r = 2,5,10$ and 20 as functions of distance from the centerline of the pipe.

With increasing adhesion (not shown), the density of the fluid in the first layer next to the wall increased, but the range of the wall effect (liquid layer with a thickness of a few lattice spacing) in the density was the same.

In Figures 4.3 and 4.4 the column height and the dynamic contact angle are shown for $r = 5$ and 20 as functions of simulation time. For comparison we also show the results with and without the presence of gravity, while $W = -0.1$ was kept constant. For increasing pipe radius there was a decrease in the column height which is expected from Eq. (4.3).

Without gravity, as expected from Eq. (4.3), the column rose faster with increasing pipe radius. Moreover, there was an increase in the column height for increasing pipe radius, which is expected. The solid lines in Figures 4.3 and 4.4 show the corresponding numerical solutions of Eq. (4.4), where the dynamic contact angle θ_d was determined from Eq. (4.8).
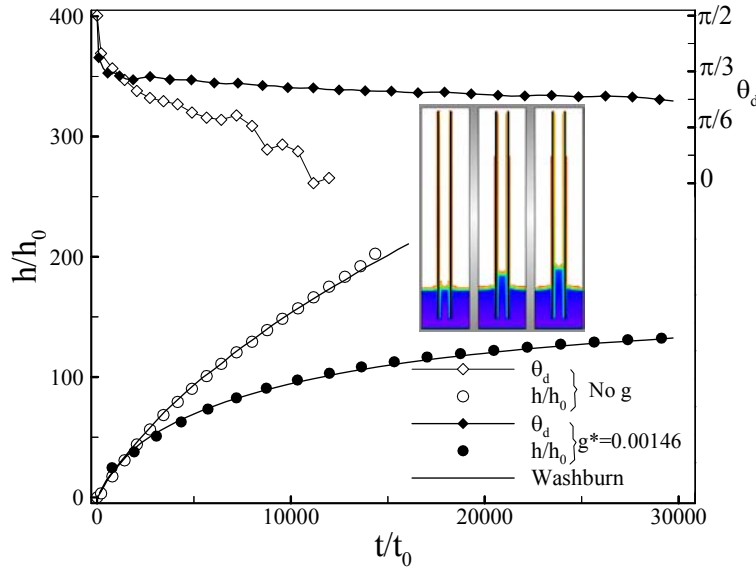
Figure 4.3 The height of the column and the dynamic contact angle as functions of simulation time for the pipe radius $r = 5$. The inset shows three snapshots of the capillary rise: initial, intermediate, and steady state (side view).
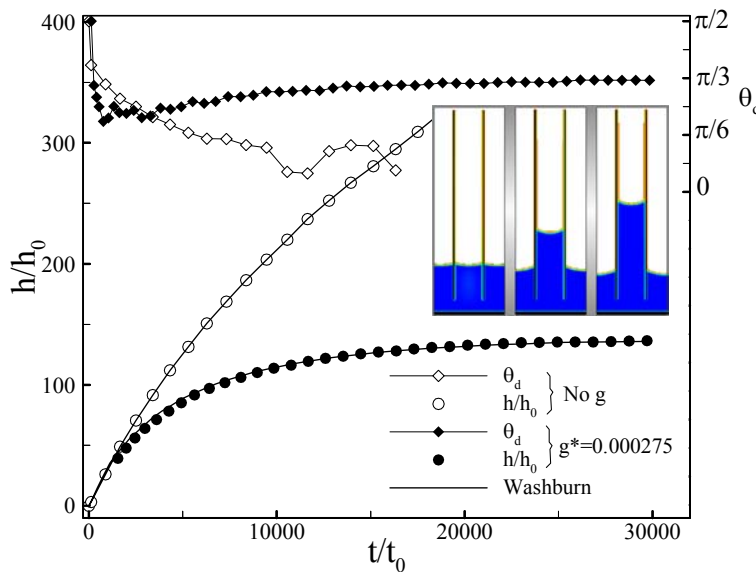

Figure 4.4 The height of the column and the dynamic contact angle as functions of simulation time for the pipe radius $r = 20$. The inset shows three snapshots of the capillary rise: initial, intermediate, and steady state (side view).

If the contact angle was kept constant, a satisfactory agreement between the Washburn equation and the simulation data could only be obtained for a short time window up to $t/t_0 \approx 1000$. On the other hand, by using θ_d in the Washburn equation as obtained from Eq. (4.8), good agreement was found for large r up to the latest data points, where some deviation appeared as a result of an increase in the interface velocity close to the end of the pipe.

At the beginning of the simulations we had $\cos\theta_d = 0$, or $\theta_d = \pi/2$, as can be seen from Figures 4.3 and 4.4. After this the contact angle θ_d decreased with increasing

time or decreasing Ca. The steady state contact angle was quickly reached, especially in the presence of gravity, in a few hundred time steps of the total simulation time of about 50 000 time steps. The increase of $\cos\theta_d$ at small Ca results from the liquid reaching the end of the pipe.

For small capillary numbers and long times, *i.e.* for slow interface velocities, θ_d approached a constant as expected. For increasing pipe radius there was an increase in the steady state contact angle, which is unphysical and is due to the difficulty of determining the precise angle from simulation results.

For stronger gravity the relative importance of the other resistive forces in Eq. (4.4) diminished, and the behaviour of θ_d was more consistent. This supports the idea that the frictional forces in our simulation model are somewhat different from those assumed in the hydrodynamical derivation of Eq. (4.8).

We also examined the speed of capillary rise as shown in Figure 4.5 as a function of time for both zero and non-zero gravity. The column first sharply speeded up and then decayed towards the stationary state approximately as $\sim t^{1/3}$. More simulation time is however needed to properly fix the exponent. While the sharp initial acceleration resulted from the fast implantation of the pipe into the system, the decay of velocity for non-zero gravity was almost independent of capillary radius.
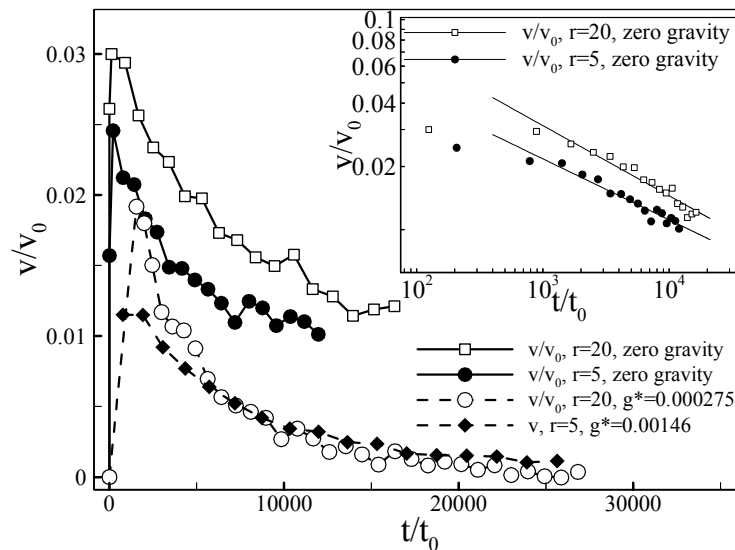

Figure 4.5 Normalized velocity of the column as a function of simulation time.

In conclusion, our test results are promising: The capillary phenomenon can indeed be studied by LBM at the hydrodynamic level. However, due to discreteness effects one needs rather thick (in lattice units) pipes for realistic kinetics. For the parametrization used here, the diameter of the pipe should be at least 30 lattice units. Future work needs to be done to validate or modify the theoretical velocity profile of a narrow capillary with strong adhesive forces at walls.

For the static properties in the presence of gravity, somewhat thinner pipes are appropriate, while thicker pipes are needed in the case of strong adhesion.

5 SOME RHEOLOGICAL PROPERTIES OF LIQUID-PARTICLE SUSPENSIONS

In this chapter I explain results for Couette flow of liquid-particle suspensions. In the simulations lattice-Boltzmann methods for the fluid (Chapter 4) and those of molecular dynamics for the Newtonian motion of solid colloidal particles (Chapter 3) are combined. The main motivation for this part of the work was to provide benchmarking for subsequent simulations on liquid-particle suspensions. We clarify the role of particle shape, shear rate, and solid volume fraction (area fraction), *i.e.* concentration, in the rheological properties of 3D (2D) suspensions. The viscosity of suspensions is analysed as a function of shear rate and concentration.

5.1 BACKGROUND

Suspensions of submicrometer-sized particles appear in many industrial processes *e.g.* in paper industry, in emulsion technology, in environmental processes, and in biological systems, to mention just a few examples [see *e.g.* 103]. There is thus wide interest in understanding the flow dynamics and rheological properties of such liquid-particle suspensions. Due to their complicated microstructure, the rheology of suspensions may depend on many factors such as particle-volume fraction, particle size, particle shape, ionization, suspending liquid, flow rate and shear rate. Recently, it has also been shown that polydispersity may have a significant effect on the hydrodynamics of particle suspensions [104,105,106]. Attractive and repulsive interactions between the particles have furthermore been found to have a significant effect on suspension's rheology [107]. One should understand better how *e.g.* particle interactions affect the rheological properties of the suspension for increasing concentration of particles, and the two-phase character of the suspension may give rise to complicated microstructural behaviour in different flow regimes.

The theoretical (both analytical and numerical) study of suspension rheology is difficult for primarily two reasons. First, the hydrodynamic interactions between the suspended particles involve several length and time scales. There are short-range lubrication forces, which are two-body interactions. There is an intermediate range in which many-body hydrodynamic interactions are important. There are also long-range interactions that must be properly 'renormalized'. Second, the exact

knowledge of the forces and stresses for a given configuration of the particles is not sufficient to determine the rheology, because an average over different particle configurations is needed. These configurations are themselves results of an interplay between the external driving forces (*e.g.* an imposed shear flow or gravity) and the 'internal' hydrodynamics, *i.e.* the inter-particle and Brownian forces. Thus, the system is completely coupled [108]. For these reasons, theoretical approaches have generally assumed highly idealized systems, such as dilute spherical suspensions at low shear rates. Experimental knowledge is also limited as the operation of even the most commonly used viscometers is not always properly under control.

Analytical and numerical studies have traditionally been based on various continuum models. However, these models always include several parameters of microscopic origin that are difficult to determine. Thus, simulation results for particulate suspensions would be most helpful and have immediate and wide applicability. On the computational side detailed analyses of microstructures have indeed become feasible through direct simulation of the motions of individual particles. Nevertheless, such studies are still computationally heavy, and usually involve approximations.

Viscosity of liquid-particle suspensions

The viscosity of a suspension of monodisperse spheres can depend on several dimensionless parameters. The most important of these are the solid volume fraction $\phi = (4/3)\pi\rho_n R^3$ and the Peclet number $Pe = \gamma_w d^2/D_0$. Here d is the particle diameter, ρ_n the particle number density, R the radius of the particles, γ_w the shear rate, and D_0 the diffusion coefficient related to the Brownian motion of the particles. The Peclet number expresses the ratio of the hydrodynamic shear forces and the diffusive Brownian forces acting on the suspended particles. The Brownian forces tend to bring the suspended particles back to their equilibrium configuration, which is continuously disturbed by the hydrodynamic shear forces acting on the particles. If the Brownian forces are omitted (as is the case here), the shear Reynolds number $\mathrm{Re}_\gamma = \rho_f d^2 u_w / (\mu_f H) = \gamma_w d^2 / v_f$ is used to characterise the flow conditions instead of the Peclet number. Here v_f is the kinematic viscosity of the carrier fluid, and ρ_f is its density. For 2D discs, *e.g.*, the area fraction is $\phi = \pi\rho_n R^2$.

The functional dependence of viscosity on ϕ and *Pe* (or Re_γ) is known theoretically only in a few limiting cases. Einstein derived at zero Reynolds number his famous formula for the relative apparent viscosity μ_r of the suspension ($\mu_r = \mu_a/\mu_f$ with μ_a the apparent viscosity of the suspension and μ_f the viscosity of the pure fluid),

$$\mu_r = 1 + \frac{5}{2}\phi. \tag{5.1}$$

Einstein omitted in his analysis the Brownian motion of the particles, and all interactions between them. For this reason Einstein's formula is only valid for very small (smaller than about 5%) solid volume fractions ϕ. When the solid volume fraction is increased, the effects of interactions between the suspended particles become significant. The inclusion of Brownian effects and hydrodynamic two-particle interactions lead to a ϕ^2 term in the expansion of the viscosity [109,110],

$$\mu_r(\gamma_w) = 1 + \frac{5}{2}\phi + k_2(\gamma_w)\phi^2. \tag{5.2}$$

Notice that μ_r now also depends on the shear rate γ_w, an effect which will become increasingly important for increasing volume fractions ϕ. This dependence is included in the factor k_2 which has the following limiting behaviour: (i) in the low-shear limit $(\gamma_w \to 0)$, where Brownian motion dominates (Region I of Figure 5.1), $k_2 = 6.2$ [110]; (ii) in the high-shear limit $(\gamma_w \to \infty)$, where hydrodynamic contributions dominate (Region III in Figure 5.1), $k_2 = 5.2$ [109]. Unfortunately, Eq. (5.2) agrees with experiments only up to volume fractions of order $15 - 20\%$. For still higher concentrations many-particle interactions must be taken into account. This is where theoretical difficulties become more severe.
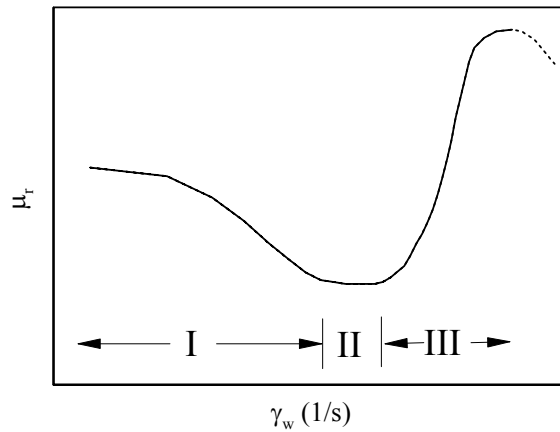

Figure 5.1 Typical viscosity of a liquid-particle suspension as a function of shear rate.

When extending the dilute-suspension analyses to higher concentrations, difficulties arise in computing the many-body hydrodynamic interactions, and in determining the configurations of the microstructure. A simple and often used expression is the relative viscosity of the (semi-empirical) Krieger- Dougherty model [111],

$$\mu_r = \left(1 - \frac{\phi}{\phi_{max}}\right)^{-\eta\phi_{max}}, \tag{5.3}$$

where η is the intrinsic viscosity of the suspension, which varies between 2.50 and 2.67 for rigid spheres depending on whether the particles are charged or not, and ϕ_{max} is the maximum packing fraction at which viscosity diverges. Experimental results of Van Der Werf and De Kruif [112] suggest that $\eta\phi_{max}$ is close to 2. The values of the maximum packing ratio ϕ_{max} which we use in scaling the volume

fraction are 0.785 (2D) and 0.605 (3D), which correspond to 'flowing' arrangements of simple cubic and hexagonal packings, respectively, perpendicular to the plane of shear [105, 112].

5.2 BENCHMARK STUDIES FOR THE LB METHOD

We carried out numerous benchmark studies to ensure the correctness and accuracy of our results and our simulation codes. As shown in Chapter 4 for fluid-flow simulations by the LB method, good agreement was found between the theoretical and simulated velocity profiles in a channel flow (see Figure 4.1). For suspension simulations an obvious test is also to compare the hydrodynamic radius R_H of particles with their nominal radius R. The hydrodynamic radius R_H was derived by simulating fluid flow through an infinite array of discs in 2D or spheres in 3D. The simulation was performed by placing a solid fixed particle in an arbitrary location in a periodic cubic box with side length L, and subject to fluid stream with velocity U. Analytical expressions for the drag coefficient are known for both 2D and 3D systems [113,114], and the latter is given by

$$F_D = 6\pi\mu_f R_H U \left/ \left[\frac{1}{R_H} - \frac{2.837}{L} + \frac{4.19}{L^3} R_H^2 - \frac{27.4}{L^6} R_H^5 \right] \right. .$$
(5.4)

We showed in Ref. [III], and show here in Table 5.1, that the hydrodynamic radii of discs in 2D were systematically smaller than R, but only by less than $1/2$ a lattice point.

R	6.0	6.2	6.5	10.0	10.2	10.5
$<R_H>$	5.65	5.80	6.13	9.57	9.78	10.06

Table 5.1. Input radius R and the mean hydrodynamic radius $<R_H>$ for a regular array of disc-shaped (2D) particles placed in different locations.

The same test was carried out in 3D by locating a solid sphere in an arbitrary location in a periodic cubic box, and the mean hydrodynamic radius was found somewhat smaller than the nominal radius R (see Table 5.2). The small discrepancy both in 2D and in 3D is mostly due to our realization of the no-slip boundary condition.

R	2.50	3.80	5.00	5.50	10.00	10.50	20.00
$<R_H>$	2.42	3.67	4.99	5.27	9.77	10.39	19.79

Table 5.2. Input radius R and the mean hydrodynamic radius $<R_H>$ for a regular array of spherical particles (3D).

Furthermore, for a disc-like particle moving under an external force, such as gravity, in the middle of a channel, good agreement was found in the forces induced on the particle and the walls, between our results and those calculated by FEM or the LB method of Ref. [72] (see Table 2 in Ref. [III]).

In another benchmark study, the hydrodynamic forces on a fixed disc with forced counterclockwise rotation close to a moving wall were simulated, and compared with the results of a commercial finite-volume solver (Fluent). Simulations were carried out for several particle radii and for two different gaps between the centre of the particle and the moving wall, and the results are shown in Table 3 of Ref. [III].

We also analysed the hydrodynamic lubrication forces between two discs scattering with a non-zero impact parameter, and in central collision [III]. The simulation results were compared with the analytical results of Ref. [115]. In both cases the relaxation parameter was $\tau = 1$.

In the scattering case, the lubrication force is [115]

$$F_{Sc} = \mu_f \Delta U_t \frac{\sqrt{2}}{h_0 s^{1/2}} \left[2J + Jx_0^2 + s\left\{ \frac{5}{12}J + \frac{1}{4}x_0 + \frac{5}{24}x_0^2 + \frac{1}{4}x_0^3 \right\} + O(s^2) \right], \quad (5.5)$$

with $x_0 = \pi(s/2)^{-1/2}$, $h_0 = 1 + x_0^2$ and $J = \sqrt{2}\tan^{-1}(x_0/\sqrt{2})$. In central collision the lubrication force is given by [115]

$$F_C = \mu_f \Delta U_n \frac{3\sqrt{2}}{2s^{3/2}} \left[J + \frac{x_0}{h_0} + s\left\{ \frac{69}{40}J + \frac{29x_0}{40h_0} - \frac{x_0}{4h_0^2} \right\} + O(s^2) \right]. \quad (5.6)$$

Here $s = (D_{12} - 2R)/R$ is the relative spacing between the two particles of radius R and of centre-to-centre distance D_{12} with 1 and 2 denoting the particles, $\Delta U_t = (\mathbf{U}_1 - \mathbf{U}_2) \cdot \mathbf{t}$ with U_1 and U_2 the particle velocities and $\mathbf{t}$ a unit vector in the direction of motion of the particles, and $\Delta U_n = (\mathbf{U}_1 - \mathbf{U}_2) \cdot \mathbf{n}$ with $\mathbf{n}$ a unit vector normal to the direction of the line connecting the particles at their shortest mutual distance. The relative normalization of the analytical and simulated lubrication forces was done so that the force on a particle by the other particle is asymptotically (for large relative distances) the same independent of the method.
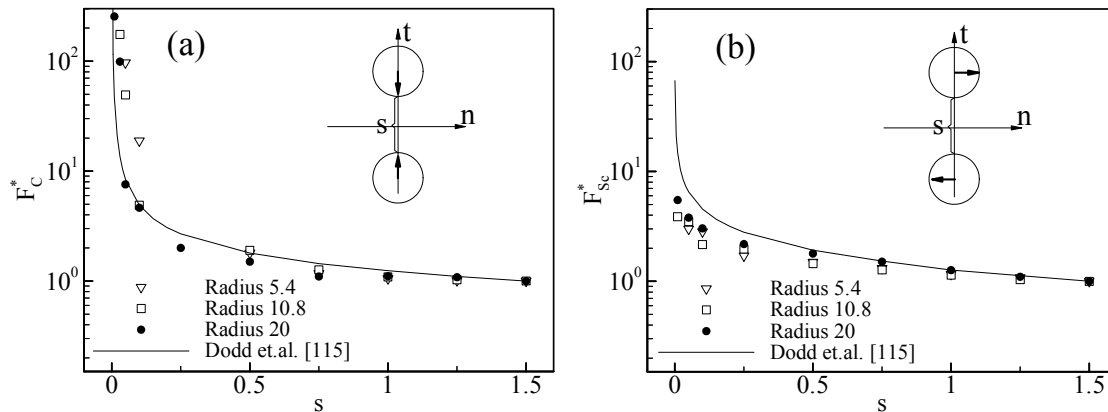

Figure 5.2 **(a)** Lubrication force on two particles in central collisions as a function of their dimensionless distance s. **(b)** Lubrication force on two particles scattering with a non-zero impact parameter as a function of the dimensionless impact parameter s. The full curves are the analytical results for the respective cases[115].

It is evident from Figure 5.2 that the simulation results are in rather good agreement with the analytical solutions. The accuracy was even better in the case of central collision and higher lattice resolutions. Similar behaviour was found in Ref. [61] for

corresponding 3D simulations. As also shown in Ref. [73], lubrication forces given by the LB method are typically smaller than the corresponding analytical predictions when particles are very close to each other (see Figure 5.2b). However, they are strong enough to keep the particles separated most of the time.

In order to test the inertial behaviour of the suspended solid particles, we also performed the lateral migration tests of Aidun and Lu [72], and Feng et. al. [116] (see Figures 5.3 and 5.4). We found good agreement with their results, when a particle initially placed near a wall migrated to the middle of the channel as shown in Figures 5.3 and 5.4 for three different ratios of partice density to fluid density. In Figure 5.4, an overshoot from the middle of the channel is also accurately reproduced by the present method.
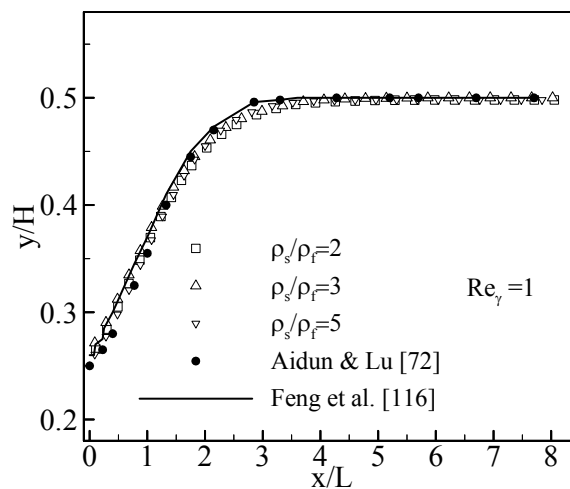
Figure 5.3 Comparison of the lateral migration of a particle in a vertical channel of length L (x direction) and width H (y direction) with the results of Aidun and Lu [72], and Feng et. al. [116], for $Re_\gamma = 1$.
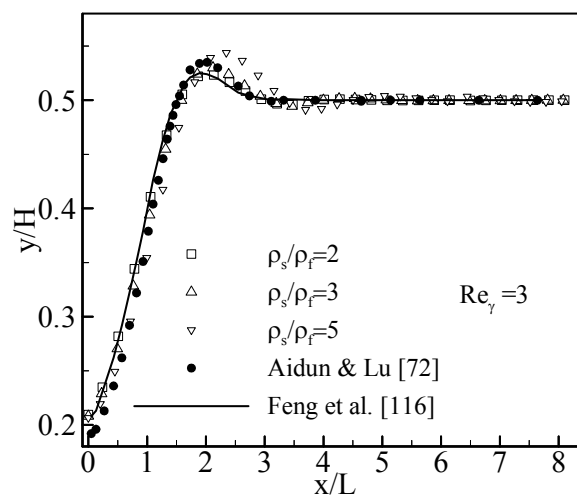

Figure 5.4 Comparison of the lateral migration of a particle in a vertical channel (the same as in Figure 5.3) with the results of Aidun and Lu [72], and Feng et. al. [116], for $Re_\gamma = 3$.

5.3   VISCOSITY OF LIQUID-PARTICLE SUSPENSIONS

In order to simulate the Couette flow of a liquid-particle suspension, suspension was placed between two moving solid walls oriented in the x direction and separated by a distance H. The walls moved with speed u_w in opposite directions. Couette-flow conditions are thus created with the mean shear rate $\gamma_w = 2u_w/H$. Periodic boundary conditions were imposed in the x direction. The simulation grid was rectangular and usually 128×128 up to 384x384 lattice points. The diameter of the particles was 10 lattice units. Volume fraction (area fraction) of the particles was varied between $\phi = 6\%$ and $\phi = 55\%$. The shear Reynolds number ($\text{Re}_\gamma = \rho_f \gamma_w d^2/\mu_f$) was varied between 0.14 and 11.7. A typical duration of the macroscopically transient states was 200 000-600 000 simulation steps depending on the system size. The necessary time-averaged quantities were calculated for the stationary states over 40 000 iteration steps, which even in the worst cases corresponded to several mean periods of a particle traversing the system.

We computed the relative apparent viscosity $\mu_r = \mu_a/\mu_f$ of the suspension. Here μ_a, the apparent viscosity of the suspension, is given by $\mu_a = \tau_T/\gamma_w$ with τ_T the total shear stress on the moving walls. We first analysed the effect of particle shape on the viscosity, and show in Figure 5.5 μ_r as a function of ϕ for disk-shaped and star-shaped particles with $\text{Re}_\gamma \approx 1.0$.

It is evident that the viscosity in the case of star-shaped particles (a cross-shaped combination of two perpendicular ellipsoidal particles, with two different axis ratios a and major axes l: $a = 4.3, l = 17.2$ and $a = 2.7, l = 8.0$) increases much more rapidly with increasing solid volume fraction than in the case of disc-shaped particles. Instead, the viscosity of ellipsoidal particles quite closely follows that of disc-like particles (not shown). Also shown in Figure 5.5 is the 2D version of the semi-emperical formula by Krieger and Dougherty [111], Eq. (5.3) with $\phi_{max} = 0.785$ and $\eta\phi_{max} = 2$.
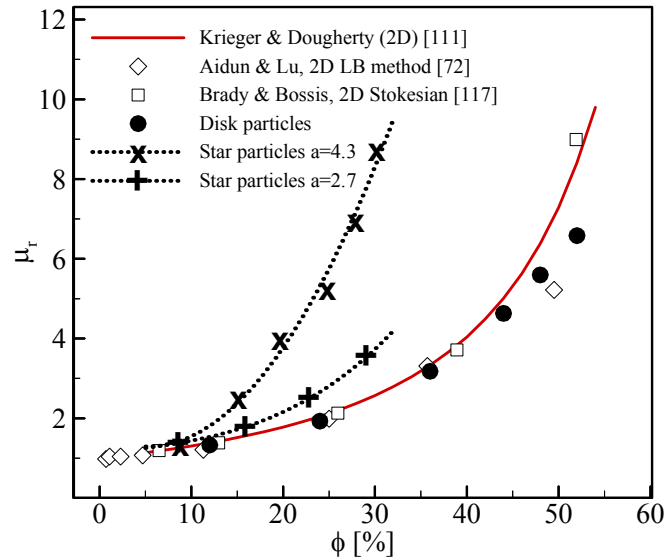
Figure 5.5 The simulated relative apparent viscosity μ_r for disk–shaped and star-shaped particles as a function of the solid volume fraction ϕ for $\mathrm{Re}_\gamma \approx 1.0$. Also shown are the semi-empirical formula by Krieger and Dougherty [111] (see Eq.(5.3)), and the simulation results of Aidun and Lu [72] and Brady and Bossis [117].

The three-dimensional Couette flow of monodispersed randomly distributed spherical particles was simulated in a fluid, which was modelled using the three-dimensional D3Q19 model with 19-links, introduced in Chapter 2. The simulation grid was 128×128, the diameter of the particles 10 lattice units, $\mathrm{Re}_\gamma = 0.1$, and volume fraction of the particles was varied between $\phi = 6\%$ and $\phi = 55\%$. A snapshot of these simulations is shown in Figure 5.6a.

A simplified version of the 3D simulation of Couette flow of monodispersed spherical particles was also carried out such that the particles were restricted to move only in one layer along the xy plane. In these monolayer simulations the shear Reynolds number was varied between 0.1 and 15, and ϕ between 6% and 52%. A snapshot of these simulations is shown in Figure 5.6b.
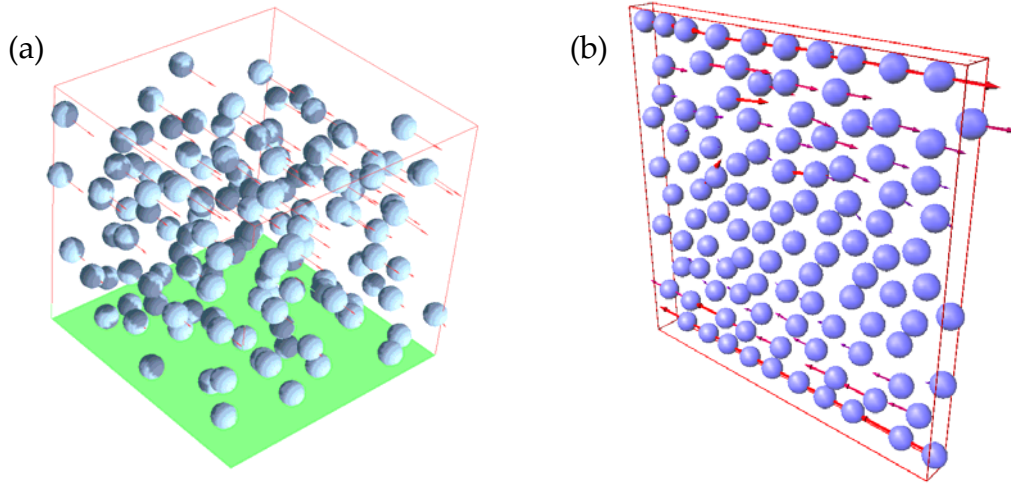
Figure 5.6 **(a)** A snapshot of a shear flow of suspended spherical particles as simulated by the three-dimensional LB method. **(b)** A snapshot of a shear flow of a monolayer of suspended spherical particles as simulated by the $3D_{(m)}$ LB method.

We computed the relative apparent viscosity μ_r of the suspension for both versions of the 3D simulations. In Figure 5.7 we show the relative apparent viscosities for $Re_\gamma = 0.1$ as functions of the scaled volume fraction ϕ / ϕ_{max} together with the 3D Krieger formula, for which $\eta \phi_{max} = 1.6$.
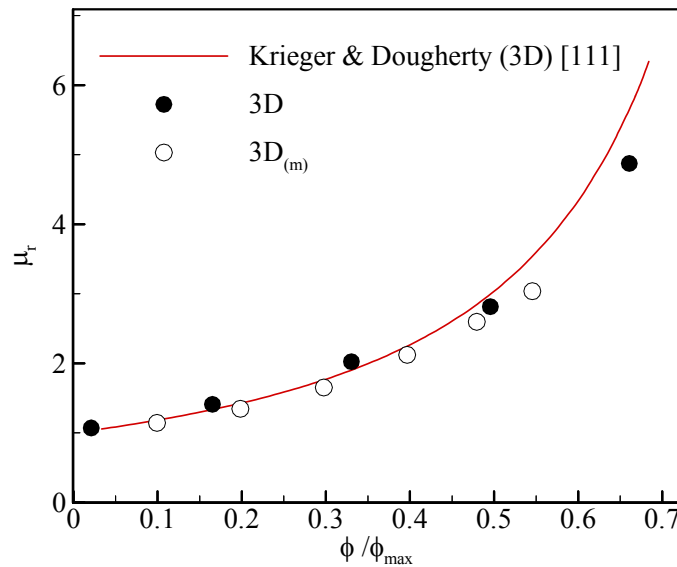

Figure 5.7 Simulated relative apparent viscosity for small Reynolds numbers, in a 3D as well as in a $3D_{(m)}$ (monolayer) system. Also shown is the 3D Krieger formula [111].

As can be seen from Figure 5.7, both 3D and $3D_{(m)}$ methods very accurately follow the Krieger formula with less than 2% deviations below $\phi / \phi_{max} \approx 0.5$.

In Figure 5.8 we compare the simulated relative viscosities of 2D and $3D_{(m)}$ suspensions for three Reynolds numbers 0.1, 1.5, and 11.7, plotted as functions of the scaled volume fraction ϕ / ϕ_{max}. Also the 2D Krieger formula is shown for comparison, and it should be applicable at low Reynolds numbers (see Eq.(5.3)).
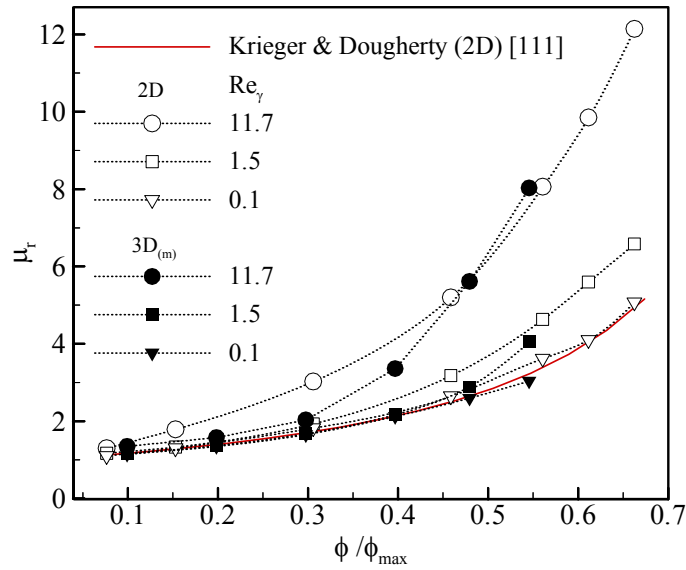
Figure 5.8 The simulated relative apparent viscosity μ_r for disk–like (2D) and spherical $3D_{(m)}$ particles restricted to move in a monolayer as a function of normalised solid volume fraction ϕ / ϕ_{max} : $\phi_{max} = 0.785$ in 2D and 0.605 in 3D. Results are shown for three values of Re_γ. Also shown is the 2D version of Krieger formula.

As shown in Figure 5.8, the magnitude of relative apparent viscosity is found to be higher in the 2D system than in a 3D monolayer of spheres for corresponding values of scaled concentration. For increasing shear rate the deviation from Krieger formula occurs at lower concentration, which is expected due to shear thickening. Note that the results for dilute $3D_{(m)}$ systems follow closely the Krieger formula, even for relatively high Reynolds numbers. For increasing solid volume fraction, the 3D relative viscosity seems to approach the corresponding 2D value.

In Figure 5.9 we show the relative apparent viscosity for $Re_\gamma = 0.1$ as a function of scaled volume fraction ϕ / ϕ_{max} together with a number of previous experimental (van der Werff and de Kruif) [112] and numerical results, all obtained for Reynolds numbers $Re_\gamma < 1$. The numerical results included in Figure 5.9 are obtained using Stokesian approximation [105, 117 ,118,119], lattice-gas simulations [120], or lattice-Boltzmann simulations [72], for both two-dimensional and three-dimensional systems. The values of the maximum packing ratio ϕ_{max} used in scaling the volume fraction were 0.785 (2D) and 0.605 (3D), as above. It is evident from Figure 5.9 that the results obtained here agree very well with the previous results shown.
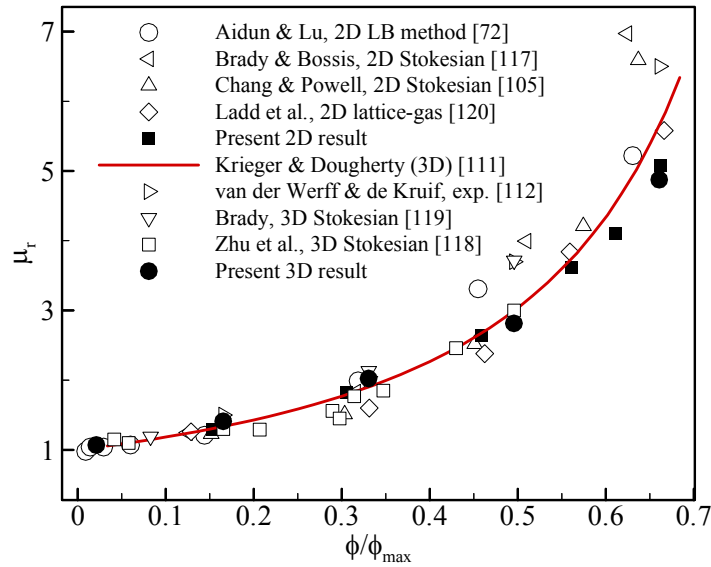
Figure 5.9 Comparison of the simulated relative apparent viscosity with previous experimental and numerical results for small Reynolds numbers, in 2D as well as 3D systems.

We also carried out several other benchmark studies such as stress distribution around a particle in shear flow, and different relative motion of particles near a wall. In addition, benchmark tests reported in Refs. [70, 71 , 73] indicate that the method applied here is adequate for realistic suspension simulations. We can conclude, based on the above tests and benchmarks, that the fundamental physical background of the model used here is correct.

6   MICROSTRUCTURE OF DILATANT SUSPENSIONS

In this chapter we analyse the 'dilatant' rheological behaviour of Couette flow of liquid-particle suspensions. The purpose of this work is to better understand the cause of shear thickening and the effects on dilatancy of the microstructure of the suspension. We study the mechanisms of momentum transfer and shear stress of liquid-particle suspensions in two dimensions using numerical simulations.

The Couette flow geometry (shear flow) of liquid-particle suspension is relevant for many applications, and appears *e.g.* in common viscometers. Often in such practical flow problems, the underlying two-phase character is neglected, and the suspension is treated as a non-Newtonian fluid. Such an approach may be useful for a dilute, homogeneous, isotropic suspension with small particles of regular shape. However, in dense suspensions their two-phase nature cannot be neglected. This is due to the importance then of other mechanisms for momentum transport in addition to viscous stress in the fluid phase. These mechanisms include particle-particle interactions and stress inside the particles. Moreover, depending on the scale of the details included, effects of boundaries or complicated microstructures such as clustering [121] and layering [122] of particles can make the two-phase flow non-homogeneous or non-isotropic.

In order to understand the underlying mesoscopic mechanisms that contribute to the total observable shear stress and consequently the apparent viscosity of a liquid-particle suspension, we compute the stresses of different phases and momentum fluxes. A snapshot of shear stress carried by the fluid can be seen in Figure 6.1, where higher shear stress areas are noticeable between solid particles. The coloured contours indicate the viscous shear stress in the fluid phase. As we concentrate here on the basic mechanisms that are responsible of the solid volume fraction and Reynolds number dependence of viscosity, we only consider the zero-gravity situation.
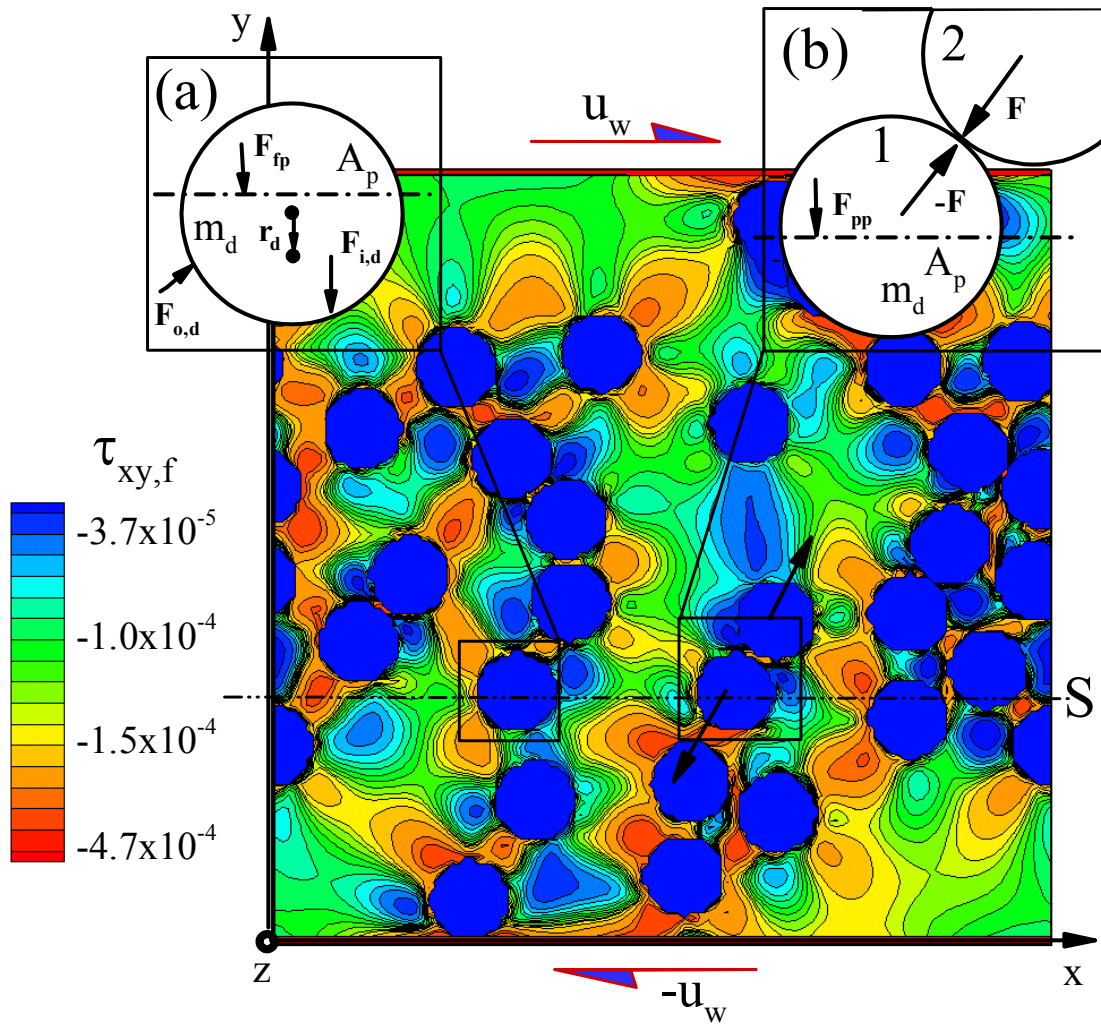
Figure 6.1 A snapshot of a two-dimensional Couette-flow of liquid-particle suspension solved by the LB method. Colour coding indicates viscous shear stress in the fluid phase. The two insets show the forces used in calculating the internal particle stress.

The Couette flow of the carrier liquid is solved using the lattice-Boltzmann method while the motion of the cylindrical (in 2D) and spherical (in 3D$_{(m)}$) particles of radius R suspended in the fluid is governed by Newtonian mechanics. The numerical technique is presented in chapter 2 and benchmarking of the simulations against results of other numerical techniques and experiments was reported in the previous chapter. The suspension is placed between two moving solid walls oriented in the x direction and separated by a distance H. The walls move with speed u_w in opposite directions. Couette-flow conditions are thus created with the mean shear rate $\gamma_w = 2u_w/H$. Periodic boundary conditions are applied in the x direction. The simulation grid is rectangular and usually of size 128x128 lattice points. In some cases lattices of size 256x256 and even 384x384 lattice points are used. The diameter of particles is 10 lattice units and their density (including the solid matrix and the core fluid) is about 3.5 times the density of the carrier fluid. We chose this particular value for the density ratio as it is relevant for pigment suspensions used in paper

coating. As discussed in the previous chapter, the results we obtain are not very sensitive to this value. Volume fraction (area fraction) of the particles is varied between 12% to 52% and the shear Reynolds number between 0.14 and 11.7. Simulations are started from a randomly distributed particle configuration (see Figure 6.1) with the fluid at rest (only walls moving).

6.1   SUSPENSION MICROSTRUCTURE IN SHEAR FLOW

In an equilibrium state, monodisperse suspensions show different structures depending on particle interactions, concentration and shear rate. For example, it is known that long range repulsion between the particles tends to order the system while short range repulsive forces lead to a fluid-like structure [107]. We first consider the effect of concentration on the microstructure of the suspension.

Figure 6.2 shows the profiles of the average velocity U of the suspension, and the local volume fraction of the particles, between the moving plates in a macroscopically stationary flow for $Re_\gamma = 1.5$, and for two systems with different volume fractions of particles. For each value of coordinate y (c.f. Figure 6.1), the average is taken over the surface S(y), over time, and over an ensemble of three macroscopically identical systems. The average velocity is calculated for the local velocity field irrespective of the phase that occupies the location. The velocity U thus represents the 'mixture velocity', *i.e.*, the total volumetric flux of the suspension in the x direction. For the relatively dilute suspension shown in Figure 6.2a, the particles seem to concentrate near the center of the channel. Weak and somewhat diffuse layering may be observed near the walls. The velocity profile slightly deviates from linear and has a shallow S shape such that the shear rate is lower near the center. This can be understood on the basis of decreased particle concentration and, consequently, lower apparent viscosity near the walls.
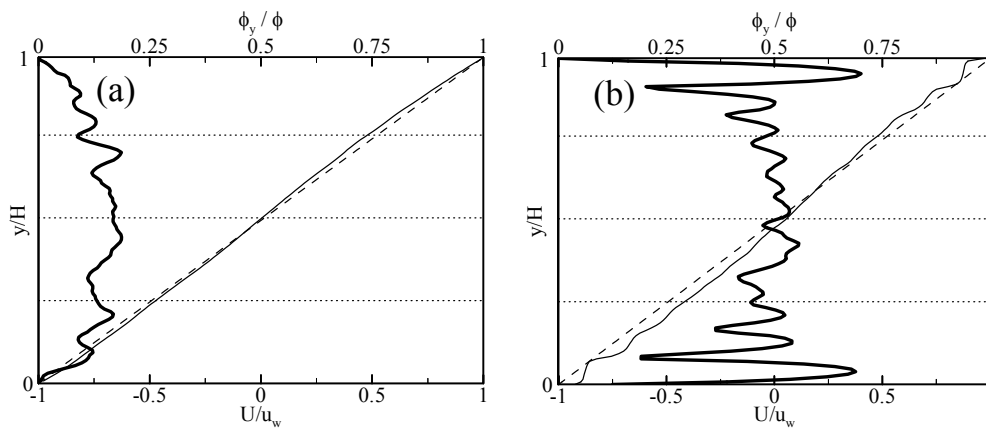

Figure 6.2 The local volume fraction of particles ϕ_y and the mean velocity profile of the suspension U across the channel width H for a suspension with $Re_\gamma = 1.5$ and mean solid volume fractions $\phi = 12\%$ **(a)** and $\phi = 48\%$ **(b)**. Thick solid line indicates the volume fraction, and thin solid line is the suspension velocity divided by the velocity of the wall (u_w). Dashed line represents a linear velocity profile.

For the denser suspension shown in Figure 6.2b, the most spectacular phenomenon is the strong layering of particles near the walls. Weaker layering is visible even in the central region of the channel. Notice that such layering was also observed in light-diffraction experiments by Hoffman [123]. The shear rate oscillates strongly near the walls, and the velocity profile seems to have features of slippage at the walls. At the central part, the shear rate is clearly lower than the average value (indicated by the slope of the dashed line). It is evident from Figure 6.2 that the mean flow of the suspension is affected by the underlying two-phase nature of the fluid.

In order to find the shear-rate dependence of layering, and the related velocity profiles, we then determined the velocity and the distribution profiles for a suspension with $\phi = 52\%$, which should display layering as indicated above, for three different shear rates. Figure 6.3a shows the local volume fraction of particles, and Figure 6.3b the mean velocity profile of the suspension. In the low shear Reynolds number region ($\mathrm{Re}_\gamma = 0.1$) the suspension is in the Newtonian flow regime, and the velocity profile is quite linear. A strong layering of particles is observed, as expected, near the walls, and it appears for all three shear Reynolds numbers. Weaker layering is visible even in the central region of the channel. Between the first layer and the wall there remains a narrow zone which contains almost entirely fluid. Experiments also often show such a layer of pure fluid in a gap less than a particle radius that decreases for increasing concentration [124].

At $\mathrm{Re}_\gamma = 1.0$ layering appears to be somewhat more pronounced near the channel walls in comparison with the two other cases. In this regime, the velocity profile starts to become nonlinear (Figure 6.3b). By increasing the shear rate beyond $\mathrm{Re}_\gamma > 1.0$, the concentration profile in the middle of the channel appears to flatten out (Figure 6.3a).
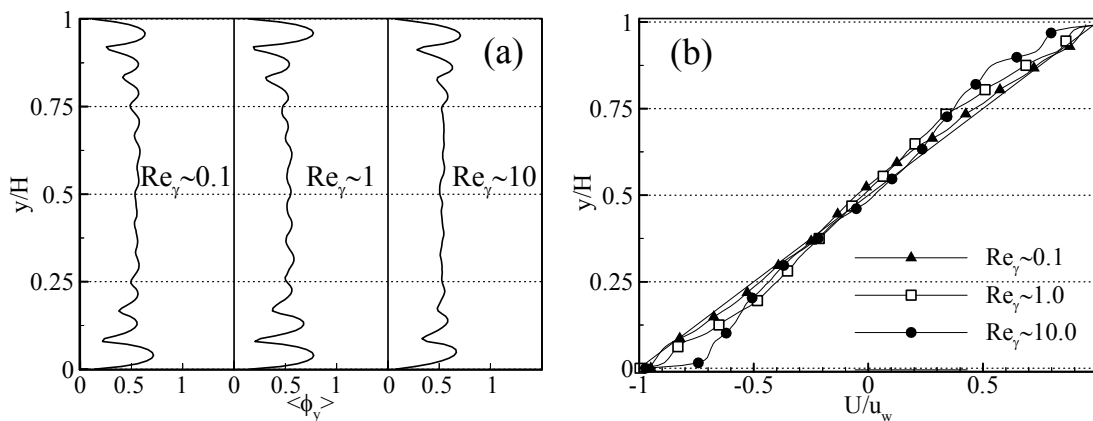

Figure 6.3 Variation of the solid volume fraction of particles **(a)**, and the mean velocity profile of the suspension **(b)**, across the channel width H for three different shear Reynolds numbers and for the mean solid volume fraction $\phi = 52\%$.

We would like to analyse in a more quantitative way the observed layering, and later also its possible relation to the apparent viscosity of the suspension. To this end

we need to quantify layering, and do this by defining a 'layering index' through a recursive procedure.

A 'layered cluster' parallel to a channel wall is composed of particles whose centres lie within a distance $\delta y = \beta R$ from the line which goes through the center of mass of the cluster and is parallel to the wall, and whose nearest-neighbour distances (between the centres of the particles) are within $\delta x = \alpha \lambda$ in the direction of the wall (see Figure 6.4). Here $\lambda = \sqrt{HL/n}$ is the 'mean free path' of the particles, n the total number of particles, and α and β coefficients that we have chosen to be $3/2$ and $1/2$, respectively. This definition is built into a recursive search routine which is continued until no new particles are found that satisfy the definition.

At first a particle is chosen at random and the layered cluster it possibly belongs to is identified. Then another (so far 'unidentified') particle is randomly chosen and the process is repeated, until all particles are 'identified'.
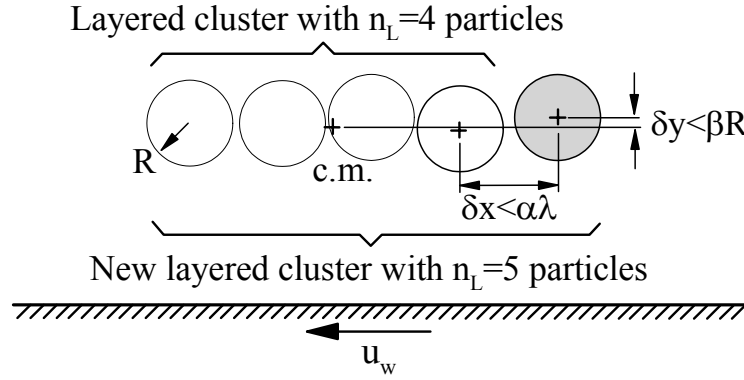

Figure 6.4 A schematic presentation of the search routine for layered clusters. A cluster of four particles is already identified, and a new particle (shaded) is then found that satisfies the criteria for the maximum horizontal distance between the nearest-neighbour centres and for the maximum distance of the centre of the particle from the horizontal line that goes through the centre of mass of the cluster. We use $\alpha = 3/2$, $\beta = 1/2$ and $\lambda = \sqrt{HL/n}$.

Here we consider only those layered clusters with $n_L > 2$ particles that are closest to the walls. We average n_L over the simulation in the stationary situation (at every 500'th time step over 200 000 time steps) and over both walls. This procedure produces a non-zero $\langle n_L \rangle$ even if all possible configurations were random distributions. We thus determine $\langle n_{L0} \rangle$ by averaging n_L over 20 independent random configurations, and subtract it from $\langle n_L \rangle$ to find layering in excess of random distribution. A 'layering index' ℓ is then defined to be

$$\ell \equiv \frac{\pi R \left(\langle n_L \rangle - \langle n_{L_0} \rangle \right)}{2L\phi}, \tag{6.1}$$

such that it is the ratio of the solid volume fraction the averaged layered cluster closest to a wall occupies of a full layer, and the solid volume fraction ϕ of the

suspension. The result of measuring this layering index ℓ for six different concentrations is shown in Figure 6.5 as a function of shear Reynolds number.
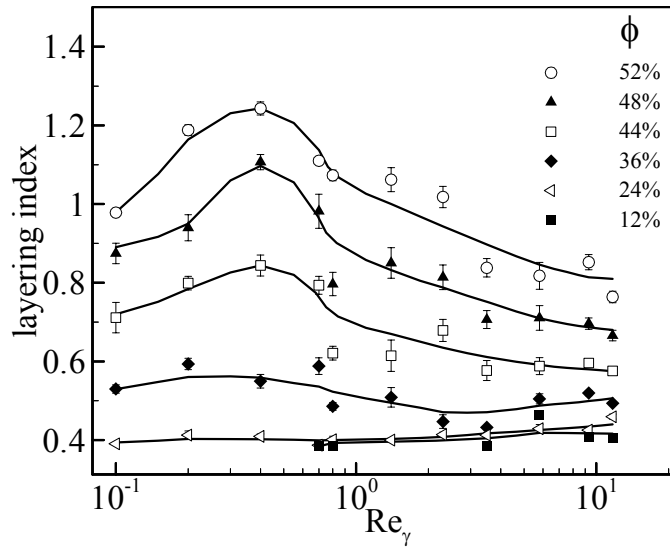

Figure 6.5 Variation of layering index ℓ as a function of shear Reynolds number for six concentrations. The solid lines are guides for the eye.

As can be seen from Figure 6.5, for increasing shear Reynolds number the layering index first increases, but then, after a maximum, it continuously decreases. This tendency is clear for concentrations above 30%, for which the maximum appears before $\text{Re}_\gamma = 1$. We might tentatively think that there are two competing effects in play here. On the one hand, an effect of walls is to suppress the rotation of nearby clusters so that they tend to align themselves along the walls. On the other hand, lubrication forces between the suspended particles tend to disorder and eventually break the clusters especially for increasing shear Reynolds numbers when even the single-phase fluid flow begins to become unstable. Whether this is indeed the relevant mechanism, we cannot tell at the moment.

This kind of behaviour resembles the decrease of 'ordering' reported by Dratler et. al. [125] in relation to shear thickening. This would also indicate that changes in the microstructure of the suspension are related to its shear thickening behaviour. It is thus instructive to also treat the suspension as a non-Newtonian single-phase fluid, and compute its apparent viscosity, as would be measured in an appropriate viscometric experiment.

6.2   SHEAR THICKENING

From the 2D simulations described above we also determined the time-averaged total shear stress on the channel walls as a function of shear rate. From the total shear stress we get the relative apparent viscosity of the suspension, and this is shown in Figure 6.6 as a function of shear Reynolds number for six concentrations. For solid volume fractions above about 30%, the relative viscosity begins to increase

with increasing shear Reynolds number at about $\mathrm{Re}_\gamma \approx 0.5$, while being more or less independent of Re_γ before that value. For lower concentrations the apparent viscosity begins to increase at higher shear rates. The dependence of apparent viscosity on Re_γ appears to be a power law (not shown here). In the corresponding $3D_{(m)}$ simulations of monolayer arrays of spheres we found very similar behaviour (see Chapter 5).
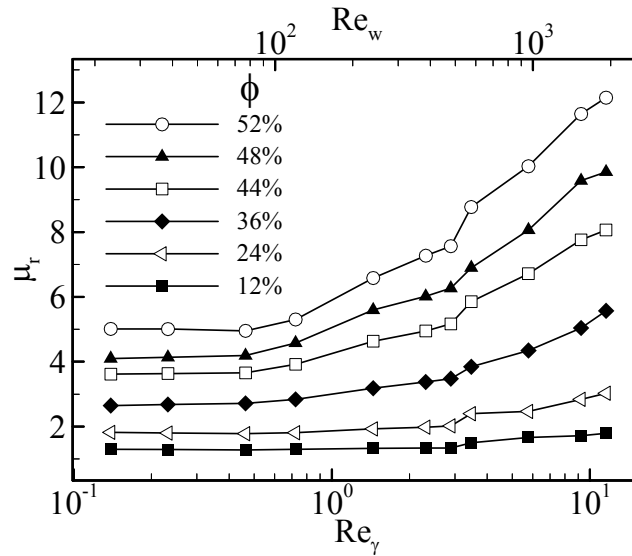

Figure 6.6 Relative apparent viscosity μ_r as a function of shear Reynolds number $\mathrm{Re}_\gamma = \rho_f d^2 u_w / \mu_f H$ for six solid volume fractions ϕ. For more information, the corresponding values of the wall Reynolds number $\mathrm{Re}_w = \rho_f u_w H / \mu_f$ are also indicated.

We can now at least partly address the question how layering is related to the relative apparent viscosity, and plot in Figure 6.7 the layering index as a function of relative apparent viscosity for the three highest solid volume fractions considered, for which layering index was found to have a maximum below $\mathrm{Re}_\gamma = 1$.
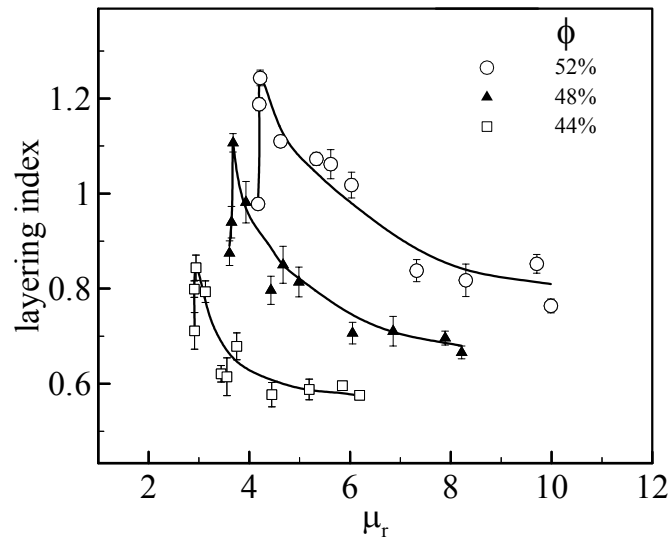
Figure 6.7 Variation of layering index ℓ as a function of relative apparent viscosity μ_r for three concentrations. Solid lines are guides for the eye.

The data points in Figure 6.7 are for different shear Reynolds numbers such that, for each concentration, Re_γ increases from left to right. It is evident from this figure that below a certain threshold value layering index is independent of μ_r, and comparison with Figures 6.5 and 6.6 reveals that this threshold roughly coincides with the maximum in the layering index and the onset of shear thickening. Above the threshold, *i.e.* in the shear thickening regime, layering index continuously decreases with increasing μ_r. We might thus conclude that disappearance of layering cannot be the cause of shear thickening, but rather that it results from a mechanism which appears to be responsible also for increasing apparent viscosity. This leads us to study the mechanisms of stress and momentum transport that contribute to the formation of viscosity.

6.3   MOMENTUM TRANSFER ANALYSIS

Momentum transfer in multi-phase systems such as particulate suspensions, is by nature a multi-scale phenomenon. We thus computed the stresses of different phases and momentum fluxes including the viscous stress in the fluid phase, the structural stress inside the particles, and the inertial fluxes that arise from the pseudo-turbulent fluctuations of both phases. The mean shear stress inside each individual particle is calculated indirectly from the hydrodynamic forces that act on the surface of the particle. Evaluation of the hydrodynamic forces acting on the particles and the stresses in the fluid phase could be done without reference to the averaged fluid-dynamical quantities such as the viscous stress tensor, because the LB method is not based on the conventional continuity and Navier-Stokes equations, but on a discretized Boltzmann equation. The details of the momentum transfer calculations are shown in chapter 2. A snapshot of the shear stress carried

by the fluid can be seen in Figure 6.1, where higher shear stress areas are noticeable between solid particles.

First we compare in Table 6.1 the different contributions to the total shear stress of the suspension.

ϕ	σ_f/τ_T	σ_s/τ_T	τ_f/τ_T	τ_s/τ_T
12%	0.013	0.057	73.98	26.03
52%	0.083	0.196	11.30	88.33

Table 6.1 Relative contributions of the different momentum transfer mechanisms to the total shear stress τ_T for two values of the solid volume fraction. Stresses σ_f and σ_s are the pseudo-turbulent stresses of the fluid and solid phases, respectively, τ_f is the viscous stress of the fluid phase, and τ_s is the shear stress in the solid phase (internal shear stress in the suspended particles).

It is evident that the convective (pseudo-turbulent) stresses are very small in comparison with the other stress terms, and need not be taken into account. Moreover, the contribution of direct collisions was also negligible (always less than 0.5% of the total stress). This is due to highly dissipative collisions between particles in our simulations.

In Figure 6.8a we show the shear stress carried by the fluid, τ_f/τ_T, and the shear stress carried by particles, τ_s/τ_T, both scaled with the total shear stress τ_T, for the solid volume fraction $\phi = 12\%$. In Figure 6.8b the same quantities are shown for $\phi = 52\%$. It is evident from Figures 6.8 that both shear stresses are nearly independent of Re_γ at low Reynolds numbers, but begin to change when the Reynolds number exceeds a threshold value that depends on the solid volume fraction. Above the threshold value, the shear stress of the solid phase increases with increasing Re_γ, while the shear stress of the fluid phase respectively decreases.

The relative contribution to the total shear stress of the solid phase seems also to strongly depend on the solid volume fraction of the suspension.
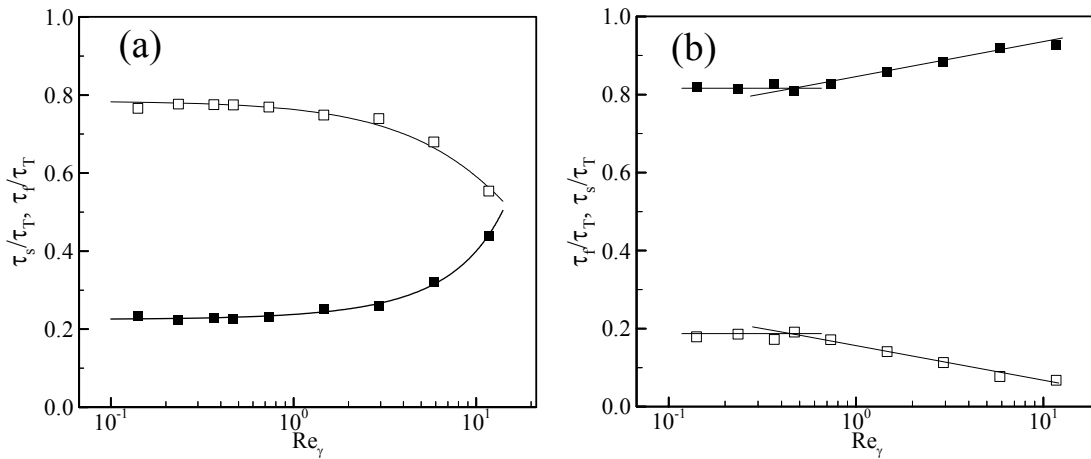
Figure 6.8 The scaled viscous (τ_f/τ_T, open squares) and solid (τ_s/τ_T, filled squares) stresses as functions of the shear Reynolds number Re_γ, for suspensions with $\phi = 12\%$ **(a)**, and $\phi = 52\%$ **(b)**. Solid lines are guides for the eye, and τ_T is the total shear stress.

To make plain the dependence on the solid volume fraction of the shear stresses, we show in Figure 6.9 both shear stresses as functions of the solid volume fraction at a fixed shear Reynolds number $\mathrm{Re}_\gamma \approx 3$.
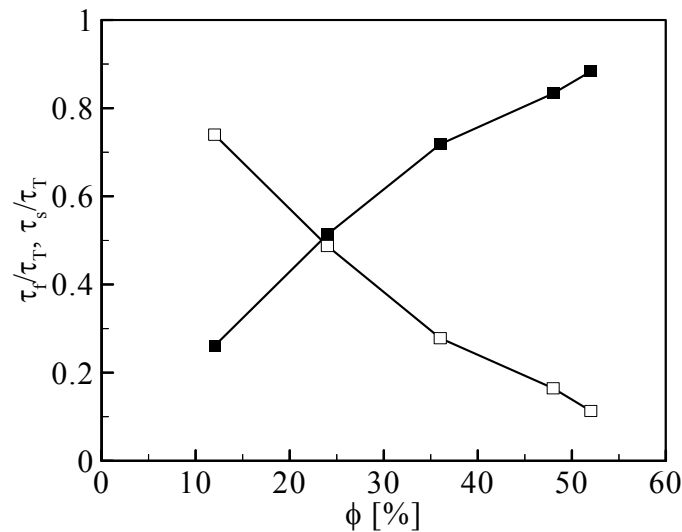

Figure 6.9 The scaled viscous (τ_f/τ_T, open squares) and solid (τ_s/τ_T, filled squares) stresses as functions of the solid volume fraction for $\mathrm{Re}_\gamma \approx 3$; τ_T is the total shear stress.

At this shear Reynolds number, the contribution of the solid phase exceeds that of the fluid phase at about $\phi = 25\%$, and at $\phi = 52\%$ the contribution of the solid phase is almost 90%. Comparison of Figures 6.6 and 6.8 indicates that, as a function of shear Reynolds number, the solid-phase contribution begins to increase roughly at the onset of shear thickening, which is also roughly where the layering index has its maximum.

As the shear stress of the solid phase appears to be an important variable, we show in Figure 6.10 the relative apparent viscosity of the suspension as a function of τ_s/τ_T, the ratio of the shear stress carried by the particles to the total shear stress. The data points in this figure correspond to shear Reynolds numbers that vary between $\mathrm{Re}_\gamma = 0.1$ and $\mathrm{Re}_\gamma = 11.7$.
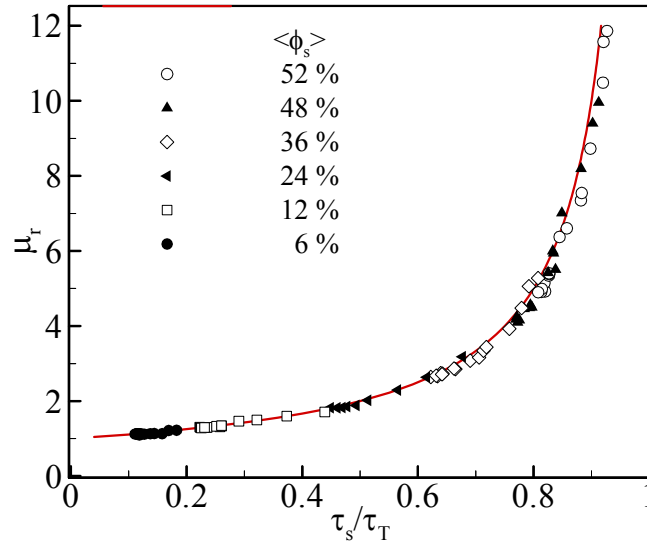

Figure 6.10 The relative apparent viscosity as a function of τ_s/τ_T for six solid volume fractions. The solid line is a fit by Eq. (6.2) to the observed values.

It is evident from Figure 6.10 that all data points collapse on a single curve, which indicates that the apparent viscosity only depends on τ_s/τ_T, and not directly on the solid volume fraction or shear Reynolds number.

From a fit to the data points we find furthermore that the scaling curve defined by the data collapse, very closely follows a simple expression

$$\mu_r = \frac{1}{1 - \tau_s/\tau_T} .$$ (6.2)

So far we have not found any explanation for this scaling form.

We can conclude by stating that the rheological behaviour of the liquid-particle suspension displays complex phenomena such as dilatancy, *i.e.* shear thickening, nonlinear velocity profile, layering of particles and apparent slip near the solid walls. A detailed study of various momentum transfer mechanisms revealed that shear thickening is related to increasing solid-phase stress, accompanied by decreasing layering near the walls. The apparent relative viscosity was found to only depend on the relative solid-phase stress, through a simple analytical expression.

7 SUSPENSION CLOGGING

7.1 INTRODUCTION

Pipe or channel blockage is a common phenomenon that may occur in a wide range of physicochemical and biological processes such as, for example, in pipeline transportation of oil or coal in a liquid [126], wheat transport in the pipes of silos, coating colour in capillary viscometer and cholesterol in human blood vessels [127]. There are two qualitatively different phenomena that may cause the blockage: jamming at high densities of suspended particles, and blockage due to growing deposited layers on channel walls. Particle deposition on channel walls narrows the flow channel and nontrivial patterns like meandering or necking of the remaining flow channel may appear. A typical example of a meandering pattern is that of rivers made by sedimentation of soil particles on riverbanks of slow streams (see *e.g.* [128,129]).

It would be of fundamental interest to find a common physical mechanism that drives the pattern formation in the above-mentioned examples as they display different patterns even though the involved physics may be rather similar. In order to analyse the basic mechanisms, we constructed a numerical model. This model should take as simple a form as possible but still capture the mechanisms that are relevant in real systems. There are two competing mechanisms in our model: Particle deposition leads to changes in the local flow velocities, which may in turn cause detachment of deposited particles.

In the simulations we applied the simplest possible attachment and detachment rules, and did not consider more complicated mechanical interactions between the particles and the flow. Large system sizes and long runs were required to obtain possible phase boundaries, and therefore we used two-dimensional simulations to get better accuracy.

We used the lattice-Boltzmann method explained above to simulate the channel flow of particle suspension [V]. When a particle touched a wall, it was assumed to get attached to it (see Figure 1.1). Mutual attachment of suspended particles were not allowed to happen. The freely floating particles should thus be understood as mesoscopic particle aggregates of the typical size of freely floating clusters. When

the total force on an attached particle (*i.e.* an aggregate) increased beyond a certain threshold value τ_P, the particle was detached and became again suspended in the liquid (c.f. Figure 7.1).
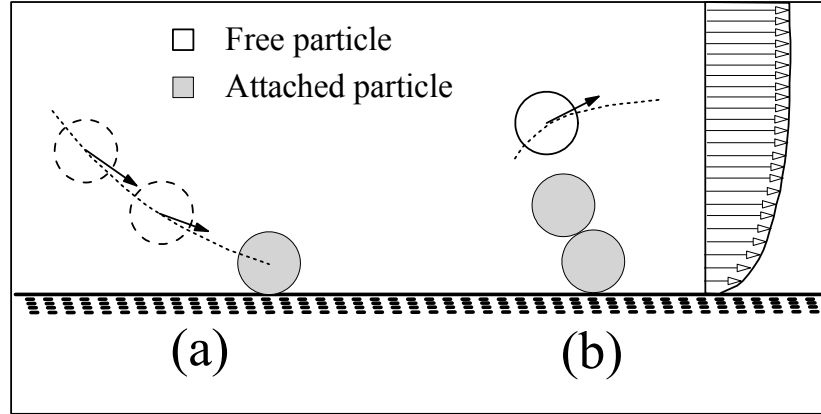

Figure 7.1 A schematic presentation of attachment **(a)** and detachment **(b)** of a particle near a channel wall.

Suspension was driven through a periodic channel of width $H \approx 30 \cdot R$ and length $L \approx 150 \cdot R$ by a pressure gradient ∇P, at low particle Reynolds numbers $\mathrm{Re}_p \leq 0.1$ (refers here to $\mathrm{Re}_p = \rho_f v 4 R^2 / \mu_f H$, where v is the velocity, ρ_f density, and μ_f viscosity of the carrier fluid.). The number of suspended particles with a diameter of $2R = 9$ lattice units varied from 500 up to 1000 ($\phi = N\pi R^2 / HL$ varied from 0.25 to 0.55), and the particle to fluid density ratio was $\rho_p / \rho_f \approx 2.5$. These particles were non-buoyant spherical discs whose mutual collisions due to the hydrodynamic lubrication forces were inelastic.

The simulation times were chosen large enough $\sim O(10^6)$ to be well in the stationary regime, where the velocity and concentration distributions used to infer the properties of the system are fully developed.

A constant pressure gradient ∇P was imposed between the inlet and the outlet by using a body force, *i.e.*, a certain momentum was added at each lattice point at each time step, including the lattice points that are inside the free and the attached particles. A particle approaching a wall was attached to the wall if its distance was less than or equal to one lattice unit from the wall or another already attached particle.

As the (dimensionless) threshold parameter we used the total force on a deposited particle normalized with the drag force on a particle near a wall,

$$\tau_P \equiv F_p^* = \frac{F_{total}}{4\pi R^2 \nabla P (H - 4R/3)}. \tag{7.1}$$

Here the total force F_{total} includes the lift and drag forces, collision forces due to other particles, and the body force. Normalization is of course arbitrary and this particular choice was made as it produces convenient values for the thresholds.

7.2 RESULTS AND DISCUSSION

For a fixed number of particles, a channel flow of suspension with deposition can be characterised by only two parameters: The solid volume fraction ϕ and the threshold τ_P [V]. If τ_P is increased from zero at a constant ϕ, we find up to six distinct regimes in the behaviour of the suspension: ordinary pipe-flow ($\tau_P \leq \tau_d$), two types of deposition in the both meandering and necking regimes, and blocking ($\tau_P > \tau_b$) (see Figures 7.2 and 7.3).

Deposition of particles began as τ_P was increased beyond a threshold value $\tau_d(\phi)$. Above this threshold curve, different types of deposition pattern were found on the channel walls. There was a non-zero region above $\tau_d(\phi)$ in which the number of deposited particles was less than the number of particles needed to block the system. This means there is an equilibrium in which a fluctuating 'interface' $h(x,t)$ at position x and time t, separates the deposited layer from the rest of the suspension on both channel walls. This 'interface' was extracted by connecting the center points of attached particles, which were locally the most distant from the wall. The resolution of the interface was therefore one particle diameter.
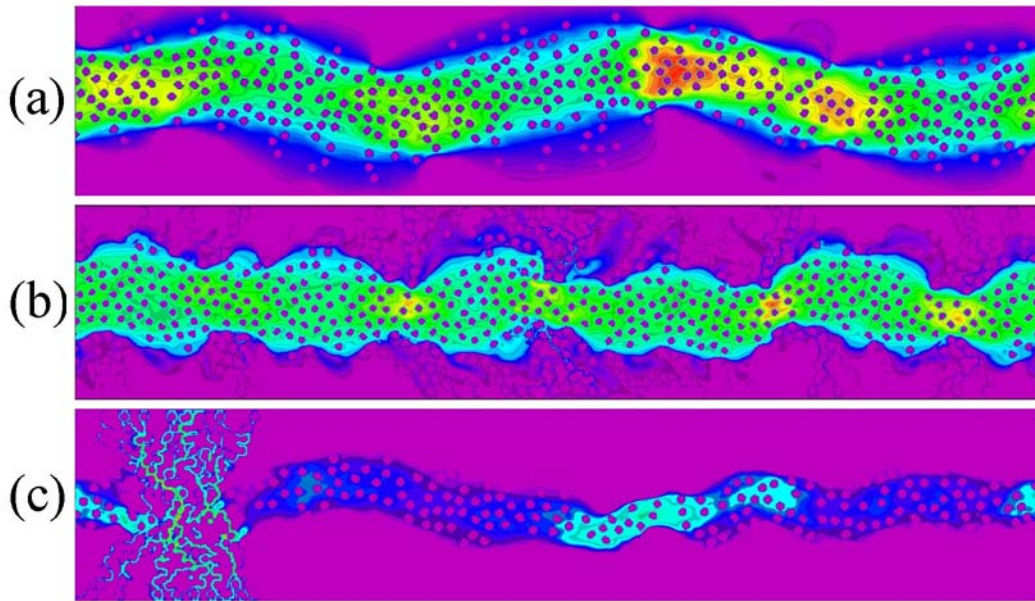

Figure 7.2 Snapshots with color coded fluid velocities (violet is zero velocity and red is high velocity). **(a)** Meandering for $\tau_P = 0.18$, $\phi = 0.26$, and $C_s = 0.11$. **(b)** Necking for $\tau_P = 0.067$, $\phi = 0.46$, and $C_s = -0.13$. **(c)** Blockage for $\tau_P = 0.095$ and $\phi = 0.46$. C_s is not defined because of blocking.

By calculating the cross correlation between the upper and lower interface curves, we could examine if they were correlated. This makes it possible to distinguish between a meandering type and a necking type of deposition. Cross correlation is defined as

$$C_s = \left\langle \frac{Cov(h_1, h_2)}{\sigma_1 \sigma_2} \right\rangle,$$

$$Cov(h_1, h_2) = n^{-1} \sum_x \left(h_1(x,t) - \overline{h}_1(t) \right) \left(h_2(x,t) - \overline{h}_2(t) \right), \qquad (7.2)$$

$$\sigma_\alpha^2 = n^{-1} \sum_x \left(h_\alpha(x,t) - \overline{h}_\alpha(t) \right)^2,$$

where σ is the standard deviation, n is the number of points at the interface curves, $\alpha = 1, 2$ refers to the upper and lower interfaces, respectively, the bar denotes average over an interface, and the angular brackets denote ensemble average.

For flow paths just above the transition ($\tau_P \geq \tau_d$), cross correlation was positive indicating a meandering type of deposition (Figure 7.2a). There was an exception at $\phi \approx 0.38$, where the intermediate region between the onset of deposition and blocking was very narrow. As τ_P approached the blocking limit $\tau_P = \tau_b$, cross correlation typically became negative, i.e. the interfaces at opposite sides of the channel were anti-correlated. This indicates a necking behaviour of the flow path. In this case fluctuations may more probably drive the two interfaces together, so that full blocking of the flow path appears (Figure 7.2c). Because of large fluctuations it is however difficult to determine the exact phase boundary between the meandering type and necking type of behaviours.

We could however construct the phase diagram by numerically determining the approximate locations of three phase boundaries, and support them by semi-analytical arguments [V]. The possible phase boundary between meandering and necking types of flow paths was difficult to determine even numerically, but we give an estimate based on cross-correlations also for that boundary (assuming that it exists). The phase diagram together with theoretical estimates for three phase boundaries are shown in Figure 7.3.
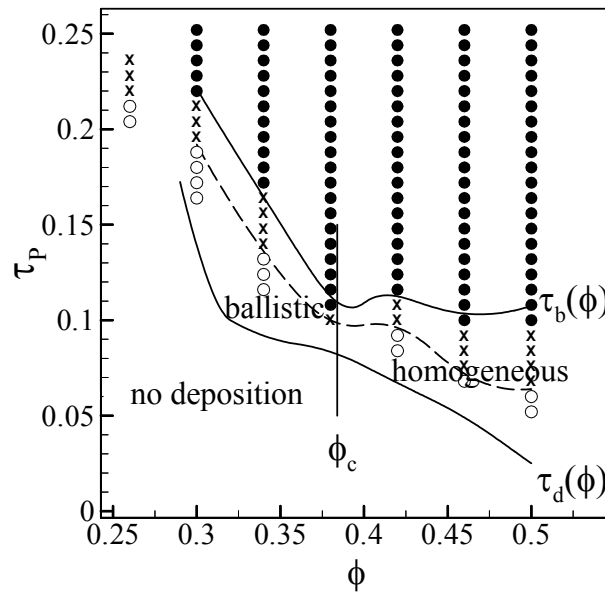
Figure 7.3 A generic phase diagram that describes the location of six phases in the (τ_P, ϕ) space. $(\bullet)$ Full blocking, $(\times)$ deposition layers with necking, $C_s < 0$, and $(\circ)$ deposition layers with meandering, $C_s \geq 0$. The dotted line is a simple spline fit between negative and positive correlations. To the left of $\phi = \phi_c$ deposition is ballistic, and to the right of it deposition layers are homogeneous. The full lines are phase boundaries given by the semi-analytical arguments described in the text.

In the phase with deposition layers at low ϕ and high τ_P, there was no detachment of particles, and columns of particles typical of ballistic deposition [130,131] without relaxation were formed. This is illustrated in Figure 7.4a.

At high ϕ and low τ_P, the system was characterised by rapid attachment and detachment events, which, after extensive rearrangements, resulted in more or less homogeneous and dense layers of deposited particles. Unlike in the case of ballistic deposition, density was higher in the deposited layer than in the suspension, and the thickness of the deposited layers grew until detachment and attachment events were in balance (Figure 7.4b). Finally, at high ϕ and high τ_P, rapid deposition occurred until the channel became fully blocked (Figure 7.2c).

We found that the concentration of the suspension and the deposited layers ϕ_s and ϕ_d, respectively, did not depend much on τ_P within the used flow regime, and that they crossed at $\phi = \phi_c \approx 0.38$, which thus marks the transition from ballistic to homogeneous deposition (see Figure 7.4c).
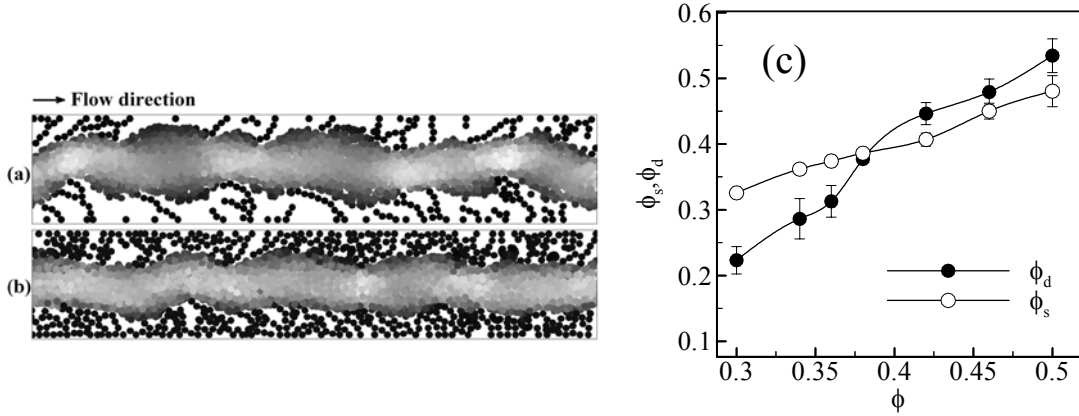
Figure 7.4 Superimposed snapshots with grey scale coded *particle velocities* regardless of fluid contours (white is high particle velocity and black is zero particle velocity). **(a)** Ballistic type of deposition, $\tau_P = 0.14$, $\phi = 0.3$, and $\phi_d/\phi_s \approx 0.76$. **(b)** Dense and homogeneous deposition layers for $\tau_P = 0.053$, $\phi = 0.5$, and $\phi_d/\phi_s \approx 1.15$. **(c)** The average concentration of particles in the deposited layers ϕ_d and the concentration of suspended particles in the flow channel ϕ_s, as functions of the solid volume fraction ϕ for $\tau_P = 0.1$.

The boundary for the onset of deposition (τ_d) was estimated by $\dot{N}_a = \dot{N}_{det}$, where $\dot{N}_a$ and $\dot{N}_{det}$ are the attachment and detachment rates, respectively. Obviously when $\dot{N}_{det} > \dot{N}_{at}$, there is no deposition. $\dot{N}_{at}$ is proportional to the rate of collisions between particles and walls, which can be determined numerically by preventing attachment in the suspension. On the other hand, $\dot{N}_{det}$ is proportional to the rate at which the fluctuating total forces exceed τ_P. These forces were numerically evaluated by recording the collision forces on a single deposited particle. By equalling the two rates determined in this way, we formed the curve $\tau_d(\phi)$ shown in Figure 7.3.

It is difficult to determine numerically the nature of the onset of the deposition transition, but if we follow the asymptotic amount of net deposited particles $N_\infty = \lim_{t\to\infty} N_a(t)$, across the transition line $\tau_d(\phi)$, it looks like N_∞ has a finite jump there to a non-zero value (Figure 7.5b). Below the transition N_a increases initially due to transient deposition, but after a relatively short time reaches a maximum, and decays exponentially to zero thereafter. Above the transition the initial rise in N_a is very similar, but there is no maximum, and N_a keeps on increasing with a very long saturation time. We find in fact that this saturation is algebraic in time. This can be seen in Figure 7.5a which shows the concentration of deposited particles for different values of ϕ. Below $\phi \approx 0.38$, *i.e.* in the case of ballistic deposition, saturation is very slow because of shadowing effects [130, 131]. It is so slow that it is not possible to determine the actual time dependence of N_a with the statistics we can get from the extremely long simulations needed in this case. On the other hand,

in the case of homogeneous deposition for $\phi \gtrsim 0.38$, we find the best fit is given to the simulated behaviour by

$$N_a(t) \approx \frac{N_\infty}{1 + c/\sqrt{t^*}}, \tag{7.3}$$

in which $t^* = tH\nabla P/2\mu_f$ is a dimensionless time, and c is a (fitting) parameter with an approximate value of $c \approx 0.8 N_{tot}$; N_{tot} is the total number of particles in the system.
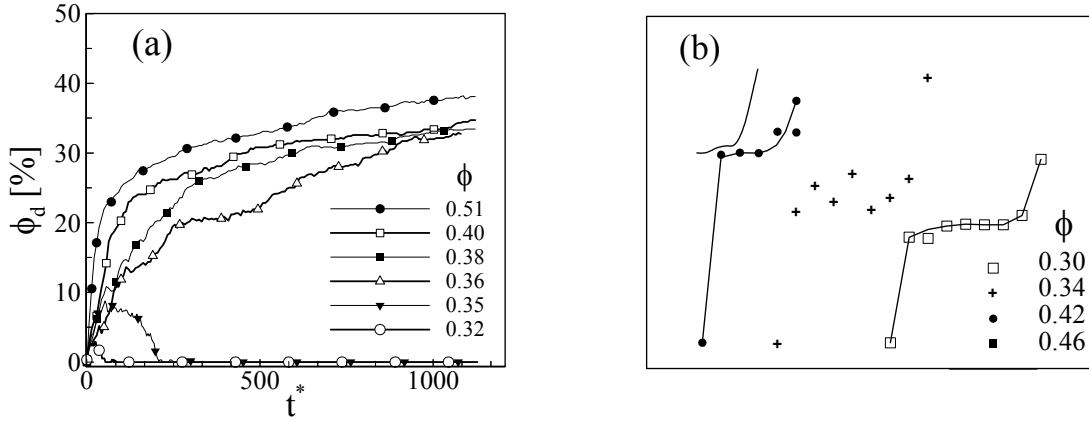

Figure 7.5 **(a)** Net deposition concentration as a function of dimensionless time for different suspension concentrations for $\tau_P = 0.085$; $t^* = t H\nabla P/2\mu_f$. **(b)** Variation with τ_P of the ratio of the asymptotic value of the attached particles N_∞ and the total number of particles N_{tot}, for the range of τ_P between no deposition and complete blocking.

In order to better analyse the clogging transition, we also considered the nature of fluctuations in the interfaces. It is evident that hydrodynamical drag forces are biggest near the local maxima in the deposited layers, and that they are lowest near the local minima. Likewise it is evident that, if we consider the height of the interface $h(x,t)$, hydrodynamical effects appear as random attachment and detachment events. For the time evolution of the interface, we are thus lead to the following (Langevin) equation,

$$\frac{\partial h(x,t)}{\partial t} = \nu\nabla^2 h(x,t) + \eta(x,t), \tag{7.4}$$

in which $\nu\nabla^2 h(x,t)$ describes the prevalent attachment and detachment events at the interface, and $\eta(x,t)$ is an effective noise term. The noise term here is assumed to have a Gaussian distribution and to be uncorrelated.

There is no mechanism in the system, which would drive locally the interface in the direction of the normal, nor is there any direct diffusion in the deposited layers. We do not thus expect there should be in this equation nonlinear terms, such as the one in the Kardar-Parisi-Zhang equation [132], or higher order derivatives of h [133]. Equation (7.4) describes equilibrium fluctuations of an interface, as it should in the present case, and is known as the Edwards-Wilkinson equation (EW)[134].

The scaling properties of the EW equation can be discussed by considering the interface fluctuation as a function of time and space $\delta h(x,t) \equiv h(x,t) - \bar{h}(t)$, where $h(x,t)$ is the height of the interface at point x and time t, and the bar denotes an average over the interface. Due to the large fluctuations of the system, it is useful to consider the two-point height-difference correlation functions

$$C(r,t) = \left\langle \left[\delta h(r+x,t'+t) - \delta h(x,t') \right]^2 \right\rangle_{x,t'}, \tag{7.5}$$

where the brackets denote an average over all configurations in time and space. In the stationary state the spatial and temporal height correlation functions have the scaling forms

$$\begin{aligned} C(r,0) &\sim r^{2\chi}, \\ C(0,t) &\sim t^{2\beta}, \end{aligned} \tag{7.6}$$

in which χ is the so-called roughening exponent and β the so-called growth exponent. We find that in our system $\beta \simeq 0.25$ independent of the size of the channel (see Figure 7.6a). This result is in agreement with that for the EW equation [135]. The results for the spatial correlation function $C(0,t)$ as shown in Figure 7.6b are not conclusive as the scaling regime is very short in this case, but they are not inconsistent with $\chi \simeq 0.5$. The higher apparent exponent at short length scales arises from the discreteness of the interface. For $r \sim O(10^2), C(r,0)$ levels off due to the finite length of the flow channel.
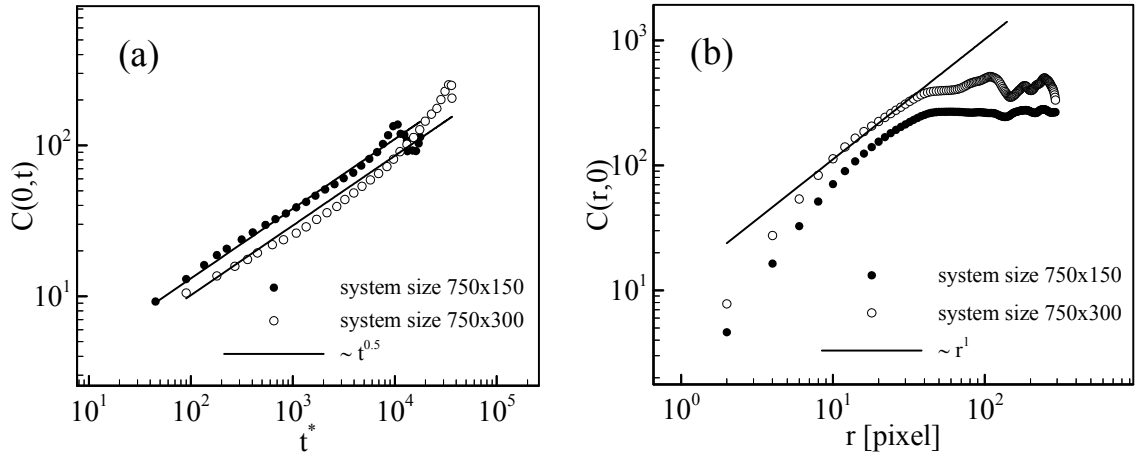

Figure 7.6 **(a)** The temporal height correlation function $C(0,t)$ vs. normalised time for a narrow and a wide system. **(b)** The spatial height correlation function $C(r,0)$ vs. r for a narrow and a wide system. For both graphs, the solid lines indicate the slopes that correspond to the EW equation.

Another quantity of interest in relation to the interface fluctuations is the local interface width [136], which can be defined as

$$w(r,t) \equiv \sqrt{\left\langle \left[h(x,t) - \bar{h}(t) \right]^2 \right\rangle_r}, \tag{7.7}$$

in which the averaging takes place over all subsystems of size r, while the system size is L. This quantity can be expected to behave as

$$w(r,t) \sim \begin{cases} t^{\beta}, & \text{for } t < L^{\chi/\beta} \\ r^{\chi}, & \text{for } t > L^{\chi/\beta} \end{cases}. \tag{7.8}$$

The fluctuations in the width of the interface therefore behave such that $w \propto t^{1/4}$ before the saturation time $t^{*} \sim L^{\chi/\beta}$. It should be noted that the relevant length scale is here the *width* of the channel and not the length of the channel, which restricts finally the scale of possible fluctuations. Using this result and Eq. (7.3), we obtain $w \propto \sqrt{N_a}$. Evidently $h \propto N_a$, and N_a and w should reach saturation simultaneously. We can thus expect that

$$\max\left[h(x,t)\right] = \alpha_1 N_a + \alpha_2 \sqrt{N_a}, \tag{7.9}$$

in which the second term on the right-hand side is the contribution of fluctuations; α_1 and α_2 are parameters which can be determined by numerical simulations. In our simulations we found $\alpha_1 \cong 17$ and $\alpha_2 \cong 2.5$. From the relation $\max\left[h(r,t)\right] = H/2$, where H is the width of the channel, we find a curve $\tau_b(\phi)$, which should give a fairly good estimate for the transition to the fully blocked phase. This curve is also shown in Figure 7.3, and we indeed observed it follows quite closely the numerical result for the phase boundary related to the clogging transition.

We can thus conclude that the basic mechanism that drives the clogging transition is the equilibrium fluctuations in the deposition layers at the channel walls. This means also that a full description of the hydrodynamical effects, as in this work, is probably needed to determine the transition. Description of the flow of the liquid part of the suspension as a Stokes flow would perhaps underestimate the relevant fluctuations.

Our numerical results also show that an increase in the solid volume fraction increases the meandering frequency. In our model it is possible to observe the onset of meandering behaviour, even though the finite width of the channel restricts the meandering amplitude, and compare it with the previous results on unlimited river meandering [128, 129]. The relation between the characteristic wave length of meandering (λ_m) and the (suspension) flow velocity (V_s), can be used to characterise the phenomenon. According to the model calculations of Ref. [129],

$$V_s \propto \sqrt{\lambda_m}. \tag{7.10}$$

We analysed the flow path in terms of the mean value of the upper and lower interfaces of the equilibrium state, by fast Fourier transform. We chose the second largest wave length maximum of the Fourier transform to characterise the meandering wave length, and compared it with the observed fluid velocity. The result is shown in Figure 7.7. Our numerical results seem to be fairly consistent with the model predictions of [129], *i.e.* with Eq. (7.10). This means meandering in our

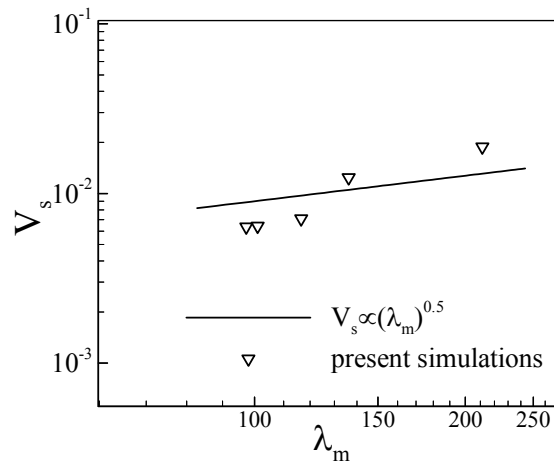simulations appears to have similar characteristics as the fully developed meandering described in [129].

Figure 7.7 Variation of suspension velocity as a function of meandering wave length.

Even though the results reported here are only a first attempt to understand channel flow with particle deposition on the walls from a microscopic fluid dynamics point of view, we expect that the basic mechanisms that we were able to clarify, will already be useful in many practical problems. The flow was only considered here at small (particle) Reynolds numbers, and one would expect even more complex behaviour to appear when the Reynolds number is increased.

8 CONCLUSIONS

In the present study, numerical techniques were used to investigate several fluid flow phenomena. Both single- and multi-phase systems were studied, by microscale MD simulations of solid particles up to mesoscopic LB simulations of liquid-particle suspensions.

In molecular dynamics simulations of dense, monosized, rough inelastic particles, the decay of diffusion coefficients along with change from disordered to layered configurations was observed, and the diffusion coefficients were also examined as functions of shear rate.

We tested the use of the lattice-Boltzmann method in studying the classical capillary rise problem in order to find if the method can be used to simulate imbibition of fluid in porous media. The results were promising and displayed the well-known capillary rise behaviour, but only for large capillary radii due to discretization problems.

An important result was the understanding gained for the shear thickening behaviour of the Couette flow of liquid-particle suspensions. These flows display complex phenomena that arise from the two-phase nature of the fluid, including a nonlinear velocity profile, layering of particles near the channel walls, and apparent slip near the walls. We found that shear thickening, *i.e.* increasing apparent viscosity of the suspension with increasing shear Reynolds numbers, arises entirely from the enhanced solid-phase momentum transfer. When the relative apparent viscosity of the suspension was plotted against the solid-phase contribution to the shear stress, all simulation points collapsed on a single scaling curve for wide range of solid volume fraction and shear Reynolds number. This scaling curve was also found to be described by a very simple function of the relative solid-phase stress.

A pipe flow of liquid-particle suspension was also considered, in which deposition of particles on pipe walls was allowed, together with detachment of deposited particles for high enough hydrodynamic forces. Two variables, solid volume fraction and detachment threshold, were shown to span a rich phase diagram for this system. For low values of these two parameters no net deposition appears, followed first by a transition to finite but non-blocking deposition layer on the walls. To begin with these deposition layers displayed a meandering patter, where

characteristic length scale was determined by suspension velocity in accordance with previous results. Increasing distance from the first transition lead to the appearance of necking features in the deposition layers, before a transition to a fully blocked flow channel took place.. This blocking transition was formed to be driven by equilibrium fluctuations in the thickness of the deposition layers.

These results are expected to be a starting point for a number of interesting and important applications in industrial as well as biological flow problems.

9 REFERENCES

I. P. Zamankhan, W. Polashenski Jr., H. Vahedi Tafreshi, A. Shakib-Manesh, P. J. Sarkomaa, Shear-Induced particle diffusion in inelastic hard sphere fluids, Phys. Rev. E **58**, R5237 (1998).

II. P. Raiskinmäki, A. Shakib-Manesh, A. Koponen, A. Jäsberg, J. Merikoski and J. Timonen, Lattice-Boltzmann simulation of capillary rise dynamics, J. Stat. Phys. **107**, 147 (2002).

III. P. Raiskinmäki, A. Shakib-Manesh, A. Koponen, A. Jäsberg, M. Kataja and J. Timonen, Simulation of non-spherical particles suspended in a shear flow, Comp. Phys. Comm. **129**, 185 (2000).

IV. A. Shakib-Manesh, P. Raiskinmäki, A. Koponen, M. Kataja and J. Timonen, Shear stress in a Couette flow of liquid-particle suspensions, J. Stat. Phys. **107**, 67 (2002).

V. A. Shakib-Manesh, J.A. Åström, A. Koponen, P. Raiskinmäki and J. Timonen, Fouling dynamics in suspension flows, Eur. Phys. J. E **9**, 97 (2002).

[1] S.L. Soo, *Multiphase flows (Science Press, Beijing, 1990).*

[2] C. Crowe, M. Sommerfeld and Y. Tsuji, *Multiphase flows with droplets and particles (CRC Press, 1998).*

[3] B.J. Alder and T.E. Wainwright, J. Chem. Phys. **27**, 1208 (1957).

[4] D.J. Evans and G. P. Morris, *Statistical Mechanics of Nonequilibrium Liquids (Academic, London, 1990).*

[5] J.M. Haile, *Molecular dynamics simulation (John Wiley & Sons, Inc., New York, 1992).*

[6] B.D. Todd and P.J. Daivis, Phys. Rev. Lett. **81**, 1118 (1998).

[7] S.B. Savage, Mechanics of rapid granular flow, Adv. Appl. Mech**. 24**, 289 (1984).

[8] P.A. Thompson and G.S. Grest, Phys. Rev. Lett**. 67,** 1751 (1991).

[9] T. Pöschel, T. Schwager and C. Salueña, Phys. Rev. E **62**, 1361 (2000).

[10] I. Pagonabarraga and D. Frenkel, J. Chem. Phys. **115,** 5015 (2001).

[11] G.R. McNamara and G. Zanetti, Phys. Rev. Lett. **61**, 2332 (1988).

[12] F. Higuera, S. Succi and R. Benzi, Europhys. Lett. **9**, 345 (1989).

[13] Y.H. Qian, D. d'Humières and P. Lallemand, Europhys. Lett**. 17**, 479 (1992).

[14] S. Chen and G.D. Doolen, Annu. Rev. Fluid Mech. **30,** 329 (1998).

[15] U. Frisch, B. Hasslacher and Y. Pomeau, Phys. Rev. Lett. **56**, 1505 (1986).

[16] *Lattice gas methods for partial differential equations*, edited by G.D. Doolen *(Addison-Wesley, Redwood City, CA, 1990).*

[17] D.H. Rothman and S. Zaleski, *Lattice Gas cellular automata (Cambridge University Press, 1997).*

[18] H. Chen, C. Teixeira and K. Molvig, Int. J. Modern Phys. C **8**, 675 (1997).

[19] K. Sankaranarayanan, I.G. Kevrekidis, S. Sundaresan, J. Lu and G. Tryggvason, Int. J. Multiphase Flow **29,** 109 (2003).

[20] S. Chen, H. Chen, D. Martnez and W Mathaeus, Phys. Rev. Lett. **67**, 3776 (1991).

[21] R. Benzi, S. Succi, M. Vergassola, Physics Reports **222,** 145 (1992).

[22] J.D.Jr. Anderson, *Computational Fluid Dynamics (McGraw Hill, New York, 1995).*

[23] P. Roach, *Computational Fluid Dynamics (Hermosa Publishing, Albuquerque, 1972).*

[24] A. Sangani and Mo. Guobiao, Phys. Fluids **6,** 1653 (1994).

[25] W.R. Bowen and A.O. Sharif, Nature **393**, 663 (1998).

[26] J.J. Gray, B. Chiang and R.T. Bonnecaze, Nature **402**, 750 (1999).

[27] Y. Huang, J. Feng and D.D. Joseph, J. Fluid Mech. **271**, 1 (1994).

[28] J. Feng and D.D. Joseph, J. Fluid Mech. **303**, 83 (1995).

[29] M.P. Allen and D.J. Tildesley, C*omputer simulation of liquids (Oxford University Press, New York, 1990).*

[30] A. Rahman, Phys. Rev. **136**, A405 (1964).

[31] R.W. Hockney and J.W. Eastwood, *Computer Simulation Using Particles (McGraw-Hill, 1981).*

[32] D.C. Rapaport, *The Art of Molecular Dynamics Simulation (Cambridge University Press, 1995).*

[33] J.P. Boon and S. Yip, *Molecular hydrodynamics (McGraw-Hill, New York, 1980).*

[34] J. Goodfellow, *Molecular Dynamics (Macmillan Press, London, 1991).*

[35] C.K.K. Lun and S.B. Savage, J. Applied Mech. **54,** 47 (1987).

[36] P. Jalali, Mass transfer and particle interactions in granular systems and suspension flows, PhD thesis, *Lappeenranta University of Technology* (2000).

[37] J.P. Hansen and I.R. McDonald, *Theory of Simple Liquids (Academic, New York, 1986).*

[38] D.R. Nelson and J. Toner, Phys. Rev. B **24**, 363 (1981).

[39] P.J. Steinhardt, D.R. Nelson and M. Ronchetti, Phys. Rev. B **28**, 784 (1983).

[40] L.D Landau and E.M. Lifshitz, *Quantum Mechanics (Pergamon, New York, 1965).*

[41] J.W. Dufty, J.J. Brey and J. Lutsko, Phys. Rev. E **65**, 051303 (2002).

[42] A. Einstein, Ann. Otol. Rhinol. Laryngol. **17**, 549 (1905).

[43] D.A. McQuarrie, *Statistical mechanics (Harper and Row, New York, 1976).*

[44] *Theory of laminar flows, edited by F.K. Moore (Princeton, New Jersey, 1964).*

[45] S. Chapman and T.G. Cowling, *The mathematical theory of non-uniform gases (3rd. edn., Cambridge University Press, 1970).*

[46] L.D. Landau and E.M. Lifshitz, *Fluid mechanics (Pergamon Press, London, 1963).*

[47] F.L. Hinton, M.N. Rosenbluth, S.K. Wong, Y.R. Lin-Liu and R.L. Miller, Phys. Rev. E **63**, 061212 (2001).

[48] L.S. Luo, Phys. Rev. E. **62**, 4982 (2000).

[49] Y.H. Qian, S. Orszag, Europhys. Lett. **21**, 255 (1993).

[50] See for instance R. Tao and J.M. Sun, Phys. Rev. Lett. **67**, 398 (1991); L.C. Davis, App. Phys. Lett. **60**, 319 (1992).

[51] C.K. Aidun, Y. Lu and E.J. Ding, J. Fluid Mech. **373**, 287 (1998).

[52] F. Higuera, J. Jiménez, Europhys. Lett. **9,** 663 (1989).

[53] See for instance B. Chopard and M. Droz, *Cellular automata modelling of physical systems (Cambridge University Press, 1998).*

[54] See for example O. Filippova and D. Hänel, Int. J. Mod. Phys. C. **9,** 1271 (1998).

[55] X. He and L.S. Luo, Phys. Rev. E **56,** 6811 (1997).

[56] Y.H. Qian, S. Succi and S. Orszag, Ann. Rev. Comp. Phys. **3**, 195 (1995).

[57] R. Benzi, S. Succi and M. Vergassola, Physics Report **222**, 145 (1992).

[58] M. Krafczyk, J. Tölke and L.S. Luo, Int. J. Modern Phys. B **17**, 33 (2003).

[59] K. Xu and K.H. Prendergast, J. Comp. Phys. **114**, 9 (1994).

[60] P.L. Bhatnagar, E.P. Gross and M. Krook, Phys. Rev. **94**, 511 (1954).

[61] O. Behrend, Phys. Rev. E **52**, 1164 (1995).

[62] A.I. Koponen, Simulation of fluid flow in porous media by lattice gas and lattice Boltzmann methods, PhD thesis, *University of Jyväskylä* (1998).

[63] B.D. Kandhai, Large scale lattice-Boltzmann simulations, PhD thesis, *Universiteit van Amsterdam* (1999).

[64] H. Chen, S. Chen and W.H. Matthaeus, Phys. Rev. A **45**, R5339 (1992).

[65] K. Xu and L.S. Luo, Int. J. Modern Phys. C **9**, 1177 (1998).

[66] J.D. Sterling and S. Chen, J. Comp. Phys. **123**, 196 (1996).

[67] G. Házi, Phys. Rev. E **67**, 056705 (2003).

[68] X. Shan and H. Chen, Phys. Rev. E **47**, 1815 (1993); Phys. Rev. E **49**, 2941 (1994).

[69] N.S. Martys and H. Chen, Phys. Rev. E **53**, 743 (1996).

[70] A.J.C. Ladd, J. Fluid Mech. **271**, 285 (1994).

[71] O. Behrend, R. Harris and P.B. Warren, Phys. Rev. E **50**, 4586 (1994).

[72] C.K. Aidun and Y. Lu, J. Stat. Phys. **81**, 49 (1995).

[73] A.J.C. Ladd and R. Verberg, J. Stat. Phys. **104**, 1191 (2001).

[74] G. Ristow, *Pattern Formation in Granular Materials* (*Springer, New York, 2000*).

[75] H.M. Jaeger, S.R. Nagel and R.P. Behringer, Phys. Today **49**, 32 (1996).

[76] H.M. Jaeger, S.R. Nagel, R.P. Behringer, Rev. Mod. Phys. **68**, 1259 (1996).

[77] J.T. Jenkins and S.B. Savage, J. Fluid Mech. **130**, 187 (1983).

[78] C.K.K. Lun, J. Fluid Mech. **233**, 539 (1991).

[79] V.R. Natarajan, M.L. Hunt and E.D. Taylor, J. Fluid Mech. **304**, 1 (1995).

[80] N. Menon and D.J. Durian, Science **275**, 1920 (1997).

[81] S.B. Savage and R. Dai, Mech. Materials **16**, 225 (1993).

[82] C.S. Campbell, Ann. Rev. Fluid. Mech. **22**, 57 (1990); C.S. Campbell, J. Fluid Mech. **348**, 85 (1997).

[83] W. Polashenski Jr., P. Zamankhan, S. Mäkiharju and P. Zamankhan, Phys. Rev. E **66**, 021303 (2002).

[84] P. Zamankhan, W. Polashenski Jr., H. Vahedi Tafreshi, P.J. Sarkomaa and C.L. Hyndman, Appl. Phys. Lett. **73**, 450 (1998).

[85] A.S. Clarke and J.D. Wiley, Phys. Rev. B **35**, 7350 (1987).

[86] C.K.K. Lun and A.A. Bent, J. Fluid Mech. **258**, 335 (1994).

[87] S.B. Savage and M. Sayed, J. Fluid Mech. **142**, 391 (1984).

[88] C.K.K. Lun, S.B. Savage, D.J. Jeffrey and N. Chepurnty, J. Fluid Mech. **140**, 223 (1984).

[89] S.S. Hsiau and Y.M. Shieh, J. Rheol. **43**, 1049 (1999).

[90] S.A. Safran, *Statistical Thermodynamics of Surfaces, Interfaces and Membranes* (*Addison-Wesley, Reading, 1994*).

[91] L.H. Tanner, J. Phys. D: Appl. Phys. **12**, 1473 (1979).

[92] M. Pasandideh-fard, Y.M. Qiao, S. Chandra and J. Mostaghimi, Phys. Fluids **8**, 650 (1996).

[93] C. Treviño, C. Ferro-Fontán and F. Méndez, Phys. Rev. E **58**, 4478 (1998).

[94] S. Betelú, B.M. Law and C.C. Huang, Phys. Rev. E **59**, 6699 (1999).

[95] M. Dubé, M. Rost and M. Alava, Europhys. J. B **15**, 691 (2000), and references therein.

[96] U. Frisch, D. d'Humières, B. Hasslacher, Lallemand, Y. Pomeau and J-P. Rivet, Complex Systems **1**, 649 (1987).

[97] D.H. Rothman, J. Geophys. Research **95**, 8663 (1990).

[98] V. Pot, C. Appert, A. Melayah, D.H. Rothman and S. Zaleski, J. Phys. II **6**, 1517 (1996).

[99] A.K. Gunstensen, D.H. Rothman, S. Zaleski and G. Zanetti, Phys. Rev. A **43**, 4320 (1991).

[100] E.W. Washburn, Phys. Rev. **17**, 273 (1921).

[101] F.M. White, *Fluid Mechanics (McGraw Hill, New York, 1993).*

[102] E. Schäffer and P. Wong, Phys. Rev. E **61**, 5257 (2000).

[103] H.A. Barnes, *Dispersion rheology: 1980 (Royal Soc. of Chem., London, 1981).*

[104] D.M.E. Thies-Weesie, A.P. Philipse and H.N.W. Lekkerkerker, J. Colloid Interface Sci. **177**, 427 (1996).

[105] C. Chang and R.L. Powell, J. Fluid Mech. **253**, 1 (1993).

[106] N.J. Wagner and A.T.J.M. Woutersen, J. Fluid Mech. **278**, 268 (1994).

[107] W. B. Russel, D.A. Saville and W. R. Schowalter, *Colloidal dispersions (Cambridge University Press, 1992).*

[108] J. Happel and H. Brenner, *Low-Reynolds Number Hydrodynamics (Kluwer, Dordrecht, 1991).*

[109] G.K. Batchelor and J.T. Green, J. Fluid Mech. **56**, 401 (1972).

[110] G.K. Batchelor, J. Fluid Mech. **83**, 97 (1977).

[111] I.M. Krieger and T.J. Dougherty, Tran. Soc. Rheol. **3**, 137 (1959); I.M. Krieger, Adv. Colloid Interface Sci. **3**, 111 (1972).

[112] J.C. van der Werff and C.G. de Kruif, J. Rheol. **33**, 421 (1989).

[113] G.W. Jackson, D.F. James, Canadian J. Chem. Engrg. **64**, 370 (1986).

[114] H. Hashimoto, J. Fluid Mech. **5**, 317 (1959).

[115] T.L. Dodd, D.A. Hammer, A.S. Sangani and D.L. Koch, J. Fluid Mech. **293**, 147 (1995).

[116] J. Feng, H.H. Hu and D.D. Joseph, J. Fluid Mech. **261**, 95 (1994).

[117] J.F. Brady and G. Bossis, J. Fluid Mech. **155**, 105 (1985).

[118] J.X. Zhu, D.J. Durian, J. Müller, D.A. Weitz and D.J. Pine, Phys. Rev. Lett. **68**, 2559 (1992).

[119] J.F. Brady, J. Chem. Phys. **99**, 567 (1993).

[120] A.J.C. Ladd, M.E. Colvin and D. Frenkel, Phys. Rev. Lett. **60**, 975 (1988).

[121] J.F. Brady and G. Bossis, Ann. Rev. Fluid Mech. **20**, 111 (1988).

[122] R.L. Hoffman, Trans. Soc. Rheol. **16,** 155 (1972); J. Colloid and Interface Sci. **46,** 491 (1974); Mater. Res. Bull. **16,** 32 (1991).

[123] R.L. Hoffman, J. Rheol. **42**, 111 (1998).

[124] R.W. Whorlow, *Rheological techniques (Ellis Horwood Ltd., Chichester, 1980*).

[125] D.I. Dratler, W.R. Schowalter and R. L. Hoffman, J. Fluid Mech. **353**, 1 (1997).

[126] P. Singh, R. Venkatesan, H.S. Fogler and N.R. Nagarajan, AICHE J. **47**, 6 (2001).

[127] S.G. Imbesi and W. Kerber, AJNT Am. J. Neuroradiol. **19**, 761 (1998).

[128] P. Meakin, T. Sun, T. Jossang and K. Schwarz, Physica A **233**, 606 (1996).

[129] B.F. Edwards and D.H. Smith, Phys. Rev. E **65**, 046303 (2002).

[130] P. Ramanlal and L.M. Sander, Phys. Rev. Lett. **54**, 1828 (1985).

[131] J. Krug, Materialwissenschaft und Werkstofftechnik. **26**, 22 (1995).

[132] M. Kardar, G. Parisi and Y.C. Zhang, Phys. Rev. Lett. **56**, 889 (1986).

[133] J. Villain, J. Phys. I **1**, 19 (1991).

[134] S.F. Edwards and D.R. Wilkinson, Proc. R. Soc. London, Ser. **A 381**, 17 (1982).

[135] P. Meakin, *Fractals, Scaling and Growth Far From Equilibrium (Cambridge University Press, 1998).*

[136] M. Siegert, Phys. Rev. E **53**, 3209 (1996).